

A 20.1 MHZ INTERFEROMETRIC RADIO
TELESCOPE FOR OBSERVATION OF
THE SUN AND JUPITER

by
Mike Roddewig

© Copyright by Mike Roddewig, 2012

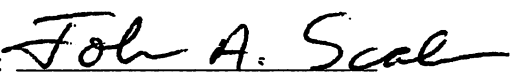
All Rights Reserved

A thesis submitted to the Faculty and the Board of Trustees of the Colorado School of Mines in partial fulfillment of the requirements for the degree of Master of Science (Engineering).

Golden, Colorado

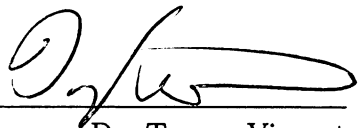
Date 8/7/12

Signed: 
Mike Roddewig

Signed: 
Dr. John Scales
Thesis Advisor

Golden, Colorado

Date 8-9-12

Signed: 
Dr. Tyrone Vincent
Professor and Interim Department Head
Department of Engineering

ABSTRACT

We have developed and built a software-defined radio telescope on the roof of our Physics department for observation of the Sun and Jupiter. The telescope is an interferometer type, with an observing frequency centered at 20.1 MHz which allowed for low-cost components to be used in the construction. A large portion of the receiver runs on FPGA, which allows for students to change the receiver architecture allowing for nearly unlimited experimentation. The entire project used open-source hardware and software.

TABLE OF CONTENTS

ABSTRACT	iii
LIST OF FIGURES	vi
LIST OF TABLES	xiii
LIST OF SYMBOLS	xiv
LIST OF ABBREVIATIONS	xv
ACKNOWLEDGMENTS	xvi
CHAPTER 1 INTRODUCTION	1
1.1 Motivation	2
CHAPTER 2 THEORY OF OPERATION	5
2.1 Effect of Bandwidth	6
CHAPTER 3 RADIO EMISSIONS FROM THE SUN AND JUPITER	11
3.1 The Radio Sun	11
3.2 Jupiter	13
CHAPTER 4 RECEIVER ARCHITECTURE	17
4.1 Antenna	18
4.2 LNA	21
4.3 Amplifier Boards	22
4.4 ADCs and Software	26
CHAPTER 5 FABRICATION AND INSTALLATION	27
5.1 Folded Dipole Antennas	27

5.2	Half-Wavelength Dipole Antennas	27
5.3	LNAs	28
5.4	Lightning Protection	32
5.5	Computer, USRP, and Amplifier Board	35
CHAPTER 6 SOFTWARE		41
6.1	telescope_usrpd	41
6.2	telescope_sqld	42
6.3	Attenuator Controller	44
CHAPTER 7 RESULTS		45
7.1	Receiver Performance	45
7.2	HVAC Noise	50
7.3	Solar Bursts	56
7.4	Jupiter Bursts	58
CHAPTER 8 CONCLUSION		71
8.1	Future Work	71
REFERENCES CITED		75
APPENDIX A - LICENSES		77
A.1	Hardware License	77
A.2	Software License	77
APPENDIX B - SCHEMATICS		79
APPENDIX C - BOARD DRAWINGS		87
CD-ROM		Pocket

LIST OF FIGURES

Figure 2.1	A basic radio interferometer. A signal is received by both antennas but one is possibly delayed relative to the other if the signal does not arrive from directly overhead. The signal from each antenna is correlated in a correlator (the multiplier and integrator) and then recorded.	6
Figure 2.2	Interferogram with baseline $B = 18$ meters. This is a theoretical plot of the interferometer response to a point-source, neglecting the effects of bandwidth.	7
Figure 2.3	Interferogram with baseline $B = 100$ meters. This is a theoretical plot of the interferometer response to a point-source, neglecting the effects of bandwidth.	8
Figure 2.4	The envelope function with baseline $B = 100$ meters and $\Delta v = 1$ MHz.	10
Figure 4.1	This mountain is located about 2 km away from our observing site. The many TV and radio transmitters proved to be a significant hindrance.	17
Figure 4.2	Folded dipole vertical radiation pattern from a simulation in 4nec2. The gain is measured in units of dBi, which is a measure of antenna directivity relative to an isotropic radiator (uniform radiation in all directions). It was not a very good antenna.	18
Figure 4.3	$\lambda/2$ dipole vertical radiation pattern. The gain is measured in units of dBi, which is a measure of antenna directivity relative to an isotropic radiator (uniform radiation in all directions). This antenna was a significant improvement on the earlier folded dipole.	19
Figure 4.4	$\lambda/2$ dipole S_{11} . This plot shows the amount of power reflected back from the antenna versus frequency. Any power not reflected back is radiated by the antenna so low S_{11} is good.	20
Figure 4.5	Simplified LNA schematic. The signal from the antenna (a) is first passed through a matching transformer (b) (this transformer was removed for the $\lambda/2$ dipole) and then each side is low-pass filtered (c) and amplified (d). Finally the signal is converted from balanced to unbalanced by a second transformer (e).	21

Figure 4.6	LNA S_{21} magnitude response. S_{21} is the forward transmission S-coefficient and is a measure of the gain of the LNA versus frequency.	22
Figure 4.7	Simplified amplifier section schematic. There are two channels, one for each antenna. From the left the signals are first passed through a band-pass filter (a) and then amplified (b). Following the first amplifier is an adjustable attenuator (c) and two more sets of amplifiers (d), (f), and band-pass filters (e), (g).	23
Figure 4.8	Amplifier board intermodulation products. All amplifiers have some non-linearities that generate signals at multiples of the input frequency. This plot shows the levels of these signals.	24
Figure 4.9	Photo of the amplifier assembly. At the rear of the shelf is the Arduino which controls the DACs. Mounted in front of it in boxes are the amplifier boards. Each board contains two sets of amplifiers and filters, the adjustable attenuator, and associated support circuitry. Two LEDs on the front indicate the status of the power supplies and a plug provides the 12 V DC input. The connectorized amplifiers on the front are connected after the amplifier boards and are followed by a pair of connectorized band-pass filters, one for each channel (not pictured).	25
Figure 5.1	One of the folded dipole antenna mounting brackets, photographed while the antenna was still in service.	28
Figure 5.2	Picture of the completed north folded dipole antenna install. The antenna is difficult to see but it follows the wall. The conduit on the right contains the coax that is connected to the LNA which is bolted to the wall.	29
Figure 5.3	The northern half-wavelength dipole. The 4x4 are weighted with cinder blocks to prevent them from blowing over. The antenna wires are very difficult to see but they are stretched between the 4x4s. The LNA is attached to the top of the middle 4x4.	30
Figure 5.4	The northern half-wavelength dipole LNA, attached to the middle 4x4. The antenna wires are simply fed through the terminal posts and then looped around. The entire assembly is generously sealed with silicone.	31
Figure 5.5	Interferogram with the new $\lambda/2$ dipole 17 meter baseline. No change is evident from the old 18 meter baseline.	32

Figure 5.6	Picture of the north LNA box as it was installed for the folded-dipoles.	33
Figure 5.7	Picture of the north LNA board installed inside its box. The mineral scale on the walls of the box is from an old water leak that we fixed.	33
Figure 5.8	The external matching transformer for the folded-dipole antennas. This was an after-thought so it was installed outside of the LNA box. We soldered wires to the transformer leads and then submerged it in marine epoxy to weatherproof it.	34
Figure 5.9	Picture of the copper ground panel. From left to right are the GPS and Ethernet surge protectors, the coaxial surge protectors, and the AC surge protector. These are all bolted to the copper ground panel. At the bottom are two ground straps, the left leads to the equipment rack and the right travels down five stories to the well in the basement of our building.	36
Figure 5.10	Picture of the equipment rack. At the top is a panel with a switch to power off the LNAs, a voltage meter connected to the 12 V bus, and a current gauge that monitors the current that the LNAs are drawing. Below them on the first shelf is the 12 V linear power supply, the bias tee board, and 12 V and ground screw terminal assembly. The next shelf down contains the amplifier assemblies. Below that is the USRP and a remote power switch which controls the power to the USRP. Both the USRP and remote power switch are connected to a network switch which is on the internal network for the telescope. Below the switch are the power-distribution unit, a power conditioner, and the UPS, and at the bottom is the computer.	39
Figure 5.11	The penthouse equipment room. The grate in the lower right-hand corner leads to a service tunnel underneath the building where we grounded the system. The sign warns that no conductive materials should be placed within 48 inches of the rack or ground panel to reduce the possibility of lightning arcing over and escaping our containment system.	40

Figure 6.1	The signal processing operations performed by the software. The multiplication is of the form $S_i \cdot S_j^*$. i and j are the channel being processed, so there are three separate signal-processing channels. The first two channels compute the power of each channel with $i = j = 1$ and $i = j = 2$. Because the channel is multiplied with its conjugate the two-norm at the end is redundant, but is used in the software to convert the <code>complex</code> type to a <code>double</code> . For the final channel we multiply $i = 1, j = 2$ which is the cross-correlation at zero-lag. In this case the result is not necessarily real so we take the two norm to compute the magnitude. In general the integrator period $t_{\max} - t_{\min}$ is 500 milliseconds but can be altered on start-up.	42
Figure 7.1	Channel 1 sensitivity testing and calibration. The signal generator was turned on at sample 30 with a power of -114 dBm and we increased the input power by 10 dB at sample 400.	46
Figure 7.2	Channel 2 sensitivity testing and calibration. The signal generator was turned on at sample 30 with a power of -114 dBm and we increased the input power by 10 dB at sample 400.	47
Figure 7.3	Phase match testing using an oscilloscope. Channel 1 is attached to the output from the receiver for the north channel and channel 2 is attached to the output from south channel. By comparing the phase of both signals we were able to determine how closely phase-matched each channel was.	49
Figure 7.4	Our antennas are located very close to the noisy HVAC equipment. The many AC induction motors in the background contributed significant RF noise to the system.	50
Figure 7.5	Coax probe S_{11} , detailing the poor performance at 20.1 MHz of the coax probe used to test for noisy equipment near our antennas.	51
Figure 7.6	Spectrum taken next to the northern antenna using the coax probe. The marker located at 20.1 MHz shows the power in a 1 Hz bandwidth.	51
Figure 7.7	Spectrum taken in the Pattridge Park parking lot using the coax probe. The marker located at 20.1 MHz shows the power in a 1 Hz bandwidth. I considered this to be an electrically “quiet” area to use as a comparison to roof where the antennas are located. . . .	52

Figure 7.8	Spectrum taken using the coax probe in the middle of Kafadar Commons, a parade field located next to our physics building. This was to see how electrically quiet the campus was in general. . .	53
Figure 7.9	One of the strong RF noise emitters is this exhaust fan, approximately 10 meters from the north antenna.	54
Figure 7.10	Spectrum taken using the coax probe next to the exhaust fan shown in the previous figure.	54
Figure 7.11	Interferometer output over an approximately 30 hour period. During this part of the year we believe the exhaust fans were being turned off at night, hence the abrupt, periodic drop in the background noise seen by the receiver.	55
Figure 7.12	Solar burst captured June 14, 2012. It lasts approximately 10 seconds, starting at 21:38:10.	57
Figure 7.13	Solar burst captured June 15, 2012. This burst was captured while an electrical storm was in the area. The lightning strikes show up as the many small spikes. The solar burst starts at approximately 20:37:30 and lasts until about 20:38:00.	58
Figure 7.14	Solar bursts captured June 27, 2012. The first burst starts at approximately 14:03 and lasts for about a minute. The second, smaller burst starts just after 14:05 and lasts for about a minute. . .	59
Figure 7.15	Solar burst captured June 27, 2012. This burst starts at about 14:18 and lasts for almost a full minute. The large spike to the left is radio-frequency interference (RFI).	60
Figure 7.16	Solar burst captured June 27, 2012. The burst starts at 12:36 and lasts for nearly two minutes. We are not sure what caused the abrupt dip in the middle.	61
Figure 7.17	Solar bursts captured June 27, 2012. This plot shows three bursts captured over a period of several minutes during a time of high RFI. The first starts at about 19:12:30 and lasts for about 30 seconds. The second starts just after 19:13 and only lasts for 15 seconds. The third burst starts just before 19:14 and lasts for about 15 seconds as well.	62

Figure 7.18	Solar bursts captured June 27, 2012. This figure shows three short bursts captured during an electrical storm. The lightning strikes show up as the many small spikes. The first solar burst starts at about 22:00:40 and lasts for about 10 seconds. The second burst starts immediately after and lasts for another 10 seconds. The third burst starts at 22:01:20 and lasts for a final 10 seconds.	63
Figure 7.19	Long solar burst captured June 28, 2012. This is a large burst that starts at 02:10 and lasts almost until 02:15. The smaller spikes super-imposed on it are probably RFI.	64
Figure 7.20	Solar bursts captured June 28, 2012, associated with an M2 flare. There are multiple, large bursts (note the scale on the left) that start at 16:05 and continue to 16:15.	65
Figure 7.21	Solar burst captured June 28, 2012. This is a strange looking burst that was captured just as the Sun was beginning to rise above the horizon.	66
Figure 7.22	Solar burst captured June 28, 2012, starting at about 21:44. This burst is associated with a C3 flare that occurred at the same time. .	67
Figure 7.23	Solar burst captured July 19, 2012. It appears that the south antenna picked up some RFI during the burst.	68
Figure 7.24	Solar burst captured July 21, 2012, starting at 17:13:45. The two spikes near the end are probably RFI. The cross-correlation channel showed a dip instead of a rise, indicating that the Sun was in one of the negative lobes of the interferometer at the time of the burst.	69
Figure 7.25	Possible Jupiter captured July 15, 2012. The Radio JOVE mailing list reported activity at this time but no plots were provided for comparison.	70
Figure 8.1	A Yagi-Uda antenna photo, published on Wikipedia. This antenna design is an ideal candidate for an improvement over the current $\lambda/2$ dipole.	73
Figure B.1	LNA Schematic	80
Figure B.2	Bias Tee Schematic	82
Figure B.3	Amp Board Schematic (RF Components)	84

Figure B.4	Amp Board Schematic (Power and Control Components)	85
Figure C.1	LNA Board Drawing	88
Figure C.2	Bias Tee Board Drawing	89
Figure C.3	Amp Board Drawing	90

LIST OF TABLES

Table 3.1	Solar Burst Types	13
Table 3.2	Major Components of Jupiter’s Decametric Emissions above 15 MHz	15
Table 7.1	Calibration constants a and b to convert the receiver output to units of flux in Jy. The calibration function is of the form $f(x) = ax + b$	48
Table B.1	LNA Bill of Materials	81
Table B.2	Bias Tee Bill of Materials	83
Table B.3	Amplifier Board Bill of Materials	86

LIST OF SYMBOLS

Baseline distance (meters)	B
Center Frequency (Hz)	ν_0
Bandwidth (Hz)	$\Delta\nu$
Instrument Delay (seconds)	τ_i
Bandwidth Factor	σ
Antenna effective aperture	A_e

LIST OF ABBREVIATIONS

Additive White Gaussian Noise	AWGN
Analog-to-Digital Converter	ADC
Central Meridian Longitude	CML
Coordinated Universal Time	UTC
Digital-to-Analog Converter	DAC
Finite Impulse Response	FIR
First In First Out	FIFO
Jansky	Jy
Low-Noise Amplifier	LNA
Pulse-per-Second	PPS
Radio-Frequency Interference	RFI
Root-Mean-Square Error	RMSE
Superior Geocentric Conjunction	SGC
Universal Software Radio Peripheral	USRP

ACKNOWLEDGMENTS

Thanks John.

CHAPTER 1

INTRODUCTION

Software-defined radio is a rapidly evolving field that has only come to fruition in the past decade. In a traditional radio receiver most of the operations take place in hardware and the receiver architecture is fixed. Any change to the receiver would require creating and constructing a new hardware design. With advances in digital electronics and field-programmable gate array (FPGA) architecture we are now able to place the majority of receiver functions in software, allowing for endless reconfigurability and experimentation. This project used a software-defined radio receiver to implement an interferometer for observations of the Sun and Jupiter. All of the hardware and software has been released as open-source material to the public and the received data will be freely accessible on the internet.

A major limitation in this project was that the telescope had to be low-cost. This influenced our choice of operating frequency. We looked at low-frequency radio astronomy, an area of radio astronomy that has been largely neglected since the 1950s. The advantages of operating at low-frequency are primarily cost. The components for the system are inexpensive and an analog intermediate frequency (IF) stage is not needed. There are several low-frequency astronomy projects currently operating including SIMPLE and Radio JOVE. 20.1 MHz was chosen for the operating frequency primarily because the Radio JOVE project operates at that frequency which would allow for sharing and collaboration with students and amateurs.

Cost also limited the location of our observatory. We chose to install it on the roof of our physics building because it had an empty mechanical shed on the top that could house the telescope equipment and was wired with data and power. The majority of our roof houses mechanical and HVAC equipment but the far end had

open space to install our antennas. Unfortunately this severely limited our baseline to only 17 meters.

Fortunately the project was successful. Although our location is significantly noisy we were still able to receive many solar emissions.

1.1 Motivation

While this project is quite similar to the Radio JOVE project and has similar goals, our system is more advanced than the JOVE receiver, although to be fair there is a significant cost difference. For many applications the JOVE receiver is quite sufficient, however, for more advanced observations a better receiver is required.

The limitations of the JOVE receiver are several. First of all it is fixed-frequency, making it impossible to observe at frequencies other than 20.1 MHz. Second it has a very small bandwidth and this, combined with the fixed receive frequency, negates the possibility of any time-frequency analysis. Third, it relies on the computer sound card ADC which has a very slow sampling rate compared to the ADC used in our receiver. This presents a (surmountable) limitation for its use as a correlating interferometer as a down-conversion is required to sample the signal located at 20.1 MHz. Our ADC is fast enough to require no down-conversion and thus no analog phase synchronization between local oscillators, as would be needed to use the JOVE receivers in a correlating interferometer (see [1]). After sampling we down-convert digitally with perfect phase synchronization between oscillators.

Most of the advanced observation possibilities from our receiver stem from the 14-bit 100 MSPS dual ADC [2] that samples the RF signal. With this high sample rate the ADC samples the entire band from DC to 50 MHz. I do not currently use anything approaching this bandwidth, mainly because this design is a first iteration and we followed the JOVE receiver design closely (although I built a correlating instead of an adding interferometer). Also I was limited by strong out of band interferers at our location which forced us to use several analog band-pass filters to prevent the RF

amplifiers from saturating on these strong interferers. These band-pass filters have only a few MHz bandwidth, centered at our nominal receive frequency of 20.1 MHz. Future designers could study these interferers more closely and attempt to improve the analog receive bandwidth, allowing us to use the full capability of the ADC.

After the ADC is an FPGA which performs several high-speed signal processing functions, one of which is the down-conversion of the RF signal to baseband. I used the default firmware provided with the receiver (cf. [3]) but future work could modify this firmware and for example perform an FFT following the ADC and to allow for a time-frequency plot to be generated. This is one of the strengths of our receiver: the majority of the receive functions are located in software as opposed to hardware, modifications and improvements are easy to make, test, and improve. As the JOVE receiver is entirely fixed in hardware, such modifications cannot be easily carried out.

Because our system functions as a correlating interferometer I have the advantage that any noise present in only one channel will not be present in the output of the cross-correlation channel. This gives us greater noise immunity than the JOVE receiver because any noise generated by the components in one channel is assumed to be uncorrelated with the opposite channel and thus will be filtered out by the correlator. Any noise generated by the components in the JOVE receiver will be present in the output as it has no way to filter out such noise.

The final advantage of our receiver is that I time-stamp our samples with GPS time in hardware with high accuracy. This allows our system to function in concert with other systems around the world as a very long baseline interferometer, because we are able to correlate our samples with other samples from other locations that are also time-stamped with GPS time.

Our location also presented many challenges that may have limited the performance of the JOVE receiver. The system had to function in the presence of strong broad-band noise and narrow-band interferers, both of which added significant chal-

lenges to the receiver design.

CHAPTER 2

THEORY OF OPERATION

This chapter is adapted from [4].

An interferometer functions by using two antennas to perform a phase comparison on a received signal (Figure 2.1). The phase of the two signals is compared via a correlation and the output of the correlator is plotted versus time. Assume we have two antennas separated by a baseline distance B meters and they receive a signal at an angle of ϕ degrees from vertical. If we designate receiver T2 as the reference receiver the time delay t_d at receiver T1 is given as

$$t_d(\phi) = \frac{B \sin \phi}{c} \quad (2.1)$$

where c is the speed of light. A negative t_d indicates that receiver T1 received the signal before receiver T2.

The baseline B has a large effect on the performance of the interferometer. For a given ϕ the output of the correlator at time t is

$$V(\phi, t) = [S(t + t_d(\phi)) \sin(2\pi v_0(t + t_d(\phi)))] \cdot [S(t) \sin(2\pi v_0 t)] \quad (2.2)$$

where S is the emitted signal and v_0 is the carrier frequency in Hertz. Rearranging and simplifying with trigonometric identities

$$V(\phi, t) = (S(t + t_d(\phi))S(t)) \left(\frac{1}{2} \cos(2\pi v_0 t_d(\phi)) - \cos(2\pi (2v_0 t + v_0 t_d(\phi))) \right) \quad (2.3)$$

We remove the $2v_0$ component using a low-pass filter leaving us with

$$V(\phi, t) = (S(t + t_d(\phi))S(t)) \left(\frac{1}{2} \cos(2\pi v_0 t_d(\phi)) \right) \quad (2.4)$$

For the moment ignore the $S(t)$ terms and focus on the cosine. In Equation (2.1) we defined $t_d(\phi)$ to be a sin term multiplied by a constant $\frac{B}{c}$. As the source moves

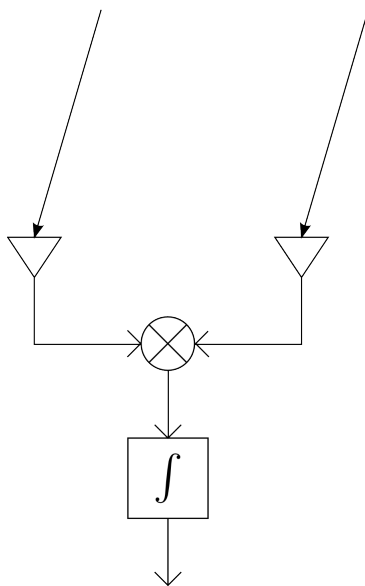


Figure 2.1: A basic radio interferometer. A signal is received by both antennas but one is possibly delayed relative to the other if the signal does not arrive from directly overhead. The signal from each antenna is correlated in a correlator (the multiplier and integrator) and then recorded.

across the sky the sin will vary from -1 to +1. Hence the cos term in Equation (2.4) will vary according to the value of the sin multiplied by the constant $\frac{2\pi\nu_0 B}{c}$. The larger the constant term the more cycles or lobes we will see in the output of the correlator. Therefore, it is important the constant term be as large as possible to have the most accuracy in determining the location of the source. However, we are limited in space on our roof and our original B was only 18 meters. At a frequency of 20.1 MHz this produces three large lobes, shown in Figure 2.2. A much better baseline such as $B = 100$ meters would produce the plot shown in Figure 2.3.

2.1 Effect of Bandwidth

Next we analyze the effect of the receive bandwidth on the interferometer response. Again consider a basic interferometer as shown in Figure 2.1 but with a time delay τ_i added to one antenna. Assume that for a point source that each antenna delivers

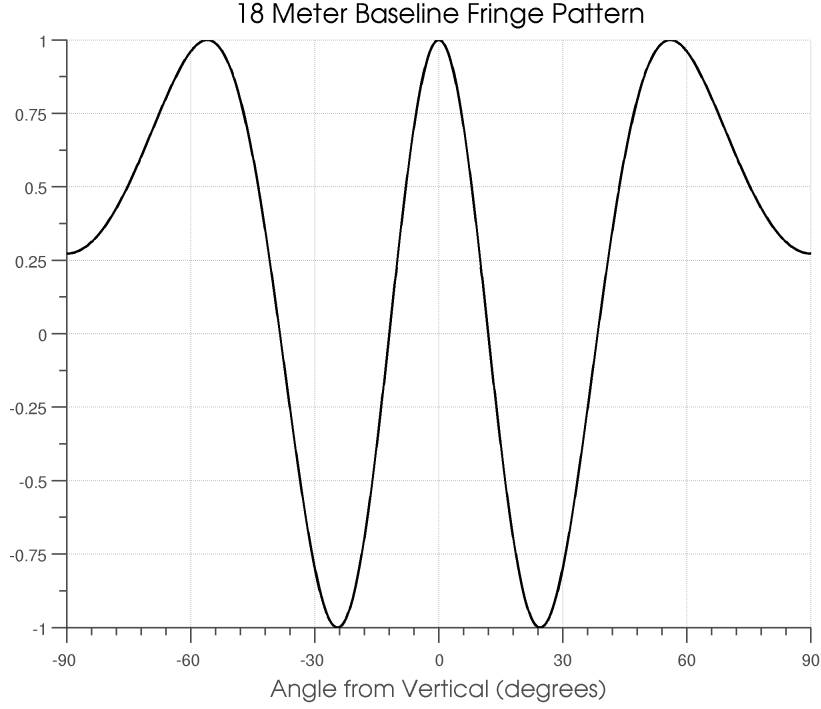


Figure 2.2: Interferogram with baseline $B = 18$ meters. This is a theoretical plot of the interferometer response to a point-source, neglecting the effects of bandwidth.

identical voltages $V(t)$ to the correlator but that one voltage lags the other by

$$\tau = t_a(\phi) - \tau_i \quad (2.5)$$

The integrator has a period of $2T$. It integrates for that period and then dumps the output and resets to zero. Thus the output of the correlator is

$$r(\tau) = \frac{1}{2T} \int_{-T}^T V(t)V(t - \tau) dt \quad (2.6)$$

We assume above that the system is ideal and the amplifiers are noiseless and have identical bandpass responses of a bandwidth $\Delta\nu$. The integration time is assumed to be much larger than $\Delta\nu^{-1}$. With this assumption we can rewrite (2.6) as

$$r(\tau) = \lim_{T \rightarrow \infty} \frac{1}{2T} \int_{-T}^T V(t)V(t - \tau) dt \quad (2.7)$$

which is the unnormalized autocorrelation function.

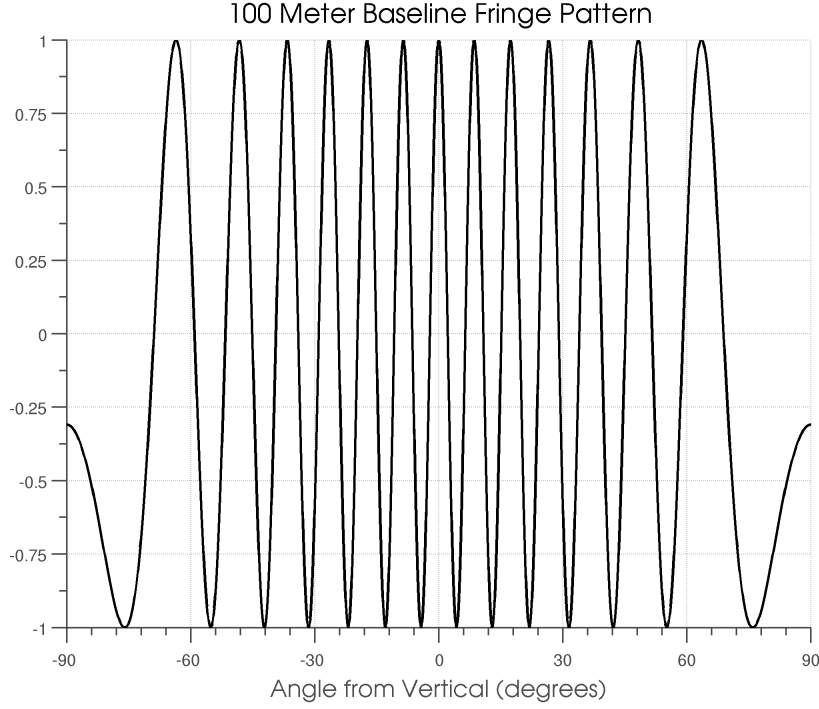


Figure 2.3: Interferogram with baseline $B = 100$ meters. This is a theoretical plot of the interferometer response to a point-source, neglecting the effects of bandwidth.

The Wiener-Khinchin theorem states that the power spectral density of a wide-sense stationary random process is the Fourier transform of its autocorrelation. Hence

$$|H(v)|^2 = \int_{-\infty}^{\infty} r(\tau) e^{-j2\pi v\tau} d\tau \quad (2.8)$$

and conversely

$$r(\tau) = \int_{-\infty}^{\infty} |H(v)|^2 e^{j2\pi v\tau} dv \quad (2.9)$$

Assume that our cosmic signal has a stationary Gaussian passband centered at v_0 . Then

$$|H(v)|^2 = \frac{1}{2\sigma\sqrt{2\pi}} \left[\exp\left(-\frac{(v-v_0)^2}{2\sigma^2}\right) + \exp\left(-\frac{(v+v_0)^2}{2\sigma^2}\right) \right] \quad (2.10)$$

where σ is the bandwidth factor. σ is related to Δv by

$$\sigma = \frac{\Delta v}{\sqrt{8 \ln 2}} \quad (2.11)$$

This signal meets the requirements of the Wiener-Khinchin theorem and we can solve (2.9) and find

$$r(\tau) = e^{-2\pi^2\tau^2\sigma^2} \cos(2\pi\nu_0\tau) \quad (2.12)$$

The cosine term is of the same form as the cosine term in (2.4) and the exponential is an envelope function whose shape and width are determined by the bandwidth and baseline. This envelope function is called the delay pattern, bandwidth pattern, or fringe washing function.

This result is quite general and shows that wide bandwidths and long baselines give a narrow fringe envelope.

For our interferometer $\Delta\nu = 100$ kHz. Because of our narrow bandwidth and small baseline the fringe envelope varies very little as a source transmits the sky so the response given by (2.12) is nearly identical to that shown in Figure 2.2. The envelope function for a 100 meter baseline with a 1 MHz bandwidth is shown in Figure 2.4.

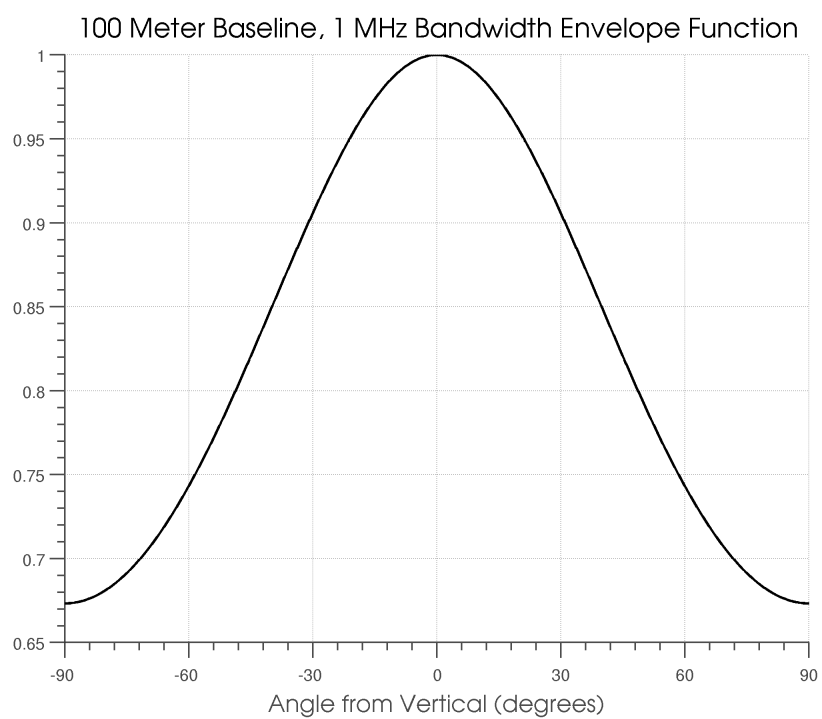


Figure 2.4: The envelope function with baseline $B = 100$ meters and $\Delta v = 1$ MHz.

CHAPTER 3

RADIO EMISSIONS FROM THE SUN AND JUPITER

This chapter is adapted from [5].

Both the Sun and Jupiter radiate in the radio spectrum but via different processes. In this chapter I will give a brief overview of the source and power of these emissions as they relate to our telescope.

3.1 The Radio Sun

Kraus divides the radio emissions from the Sun into two categories, those from the “quiet Sun” and those from the Sun in times of sunspot activity, “the disturbed Sun”. At wavelengths above 1 cm the Sun appears to follow a Planck radiation curve and radiates as a blackbody source but below 1 cm the curve branches off and the emissions are stronger than those from an equivalent blackbody source. At our wavelength of 15 meters we can expect a flux density of $\approx 10^{-23}$ W/m²/Hz from the quiet Sun.

In [6] Balanis gives a formula for the effective aperture A_e of a half-wavelength dipole

$$A_e = 0.13 \cdot \lambda^2 \tag{3.1}$$

Plugging a wavelength of 15 meters in we compute that A_e for our antenna is about 30 m². With this information and the receiver bandwidth of 100 kHz we can compute that from the quiet Sun we can expect to see a received power of -135 dBm at the antenna terminals which is far too weak for our interferometer to detect (we show that the interferometer has a sensitivity of -114 dBm in Section 7.1).

In times of sunspot activity (the “disturbed Sun”) the radiation is greatly enhanced. We can expect flux densities in the range of $\approx 10^{-18}$ W/m²/Hz. Using the

numbers from our previous calculation this is equivalent to a power at the antenna terminals of -85 dBm, which is detectable by our receiver. Kraus further divides the radiation from the disturbed Sun into two categories: the slowly-varying component and the rapidly-varying component. The slowly-varying component is not present below 3 meters so we will concern ourselves with the rapidly-varying component.

The rapidly-varying component consists of bursts which can last from seconds to hours. These bursts often appear following the appearance of a flare on the chromosphere of the Sun. These flares can last from minutes to an hour and release 10^{25} Joules of energy. There are often visible arches or prominences present after the flare event.

The radio emissions after a flare are highly variable. On the meter wavelengths there can be bursts of seconds or minutes followed by storms that last hours or days. Typically the emission first appears on higher frequencies and then moves downward to lower frequency. Wild [7] divides these events into two phases.

In Phase I Short strong bursts begin right after the visible flare, beginning at 500 MHz and moving rapidly to lower frequencies. These bursts are typically fast-drift Type III bursts with drift rates of 20 MHz/sec and a few MHz bandwidth. These bursts are theorized to be generated by plasma oscillations from the ejection of an electron jet moving at 100,000 km/sec or as a result of the chromospheric explosion of the flare. These bursts are often accompanied by continuum emissions in the meter wavelengths, believed to be generated by synchrotron emission from the electron jet. Small flares show only this Phase I sequence.

Larger flares also have a second Phase II. Phase II begins with slow-drift Type II bursts with drift rates of 20 MHz/min. Type II bursts are believed to be produced by plasma oscillations in a shock front rising ahead of an expanding gas cloud at the flare location. The gas cloud rises at 1000 km/sec which is much slower than the electron jet. Close inspection of Type II bursts shows a fine structure consistent with

a number of short Type III bursts.

Sometimes these bursts are followed by Type IV broadband, stable, continuum emissions that may last for hours or days. These emissions are assumed to be synchrotron emissions from the gas cloud at the flare location. This gas cloud rises for approximately 30 minutes, reaches a height of several solar radii, and then halts where it can remain for hours or days. At this point the emission becomes strongly circularly polarized.

Table 3.1 summarizes the burst types.

Table 3.1: Solar Burst Types [5]

Burst Type	Description
Type I	Short, narrow-band noise storm bursts.
Type II	Slow-drift bursts that move from high to low frequencies with a fundamental second-harmonic frequency structure.
Type III	Fast-drift bursts that move from high to low frequencies.
Type IV	Broadband continuum emissions.
Type V	Continuum emissions in the meter wavelengths.

3.2 Jupiter

Jupiter is an intense source of decametric (meter wavelength) radiation. This radiation is synchrotron emissions from high-energy electrons trapped outside the gaseous atmosphere of the planet. The majority of the radiation is of a circular or elliptical polarization with about 25% linear polarization. In 1964 Bigg discovered that the moon Io exerted strong control over the decametric radiation [8].

There are four easily-recognizable emission types. Io A, Io B, and Io C are all dependent on Io's phase and the fourth, non-Io A is independent. There are also Io D, Non-Io B, and Non-Io C but these are not as easy to distinguish. A given emission type is likely to occur when (1) the Jovian central meridian is within the longitude range given for the System III central meridian longitude (CML) and (2) Io's orbital

phase is close to the range given from the Superior Geocentric Conjunction (SGC). Table 3.2 summarizes these conditions.

System III maps longitude on Jupiter to the position of its magnetic field. Because Jupiter is gaseous it has no solid surface features to track its rotation and thus the magnetic field is used as the indicator of position.

The Superior Geocentric Conjunction refers to the position of Io and Jupiter as seen from Earth. The SGC is the position of Io when it is farthest from Earth on the back side of Jupiter and corresponds to an Io phase of 0° . When Io is closest to Earth with respect to Jupiter this is an Io phase of 180° .

Most of the decametric emissions are in the form of well-defined noise storms made up of groups of repeated, randomly-spaced bursts of noise (called L-Bursts) with typical durations of 1-6 seconds. L-Bursts result from scintillations resulting from drifting phase inhomogeneities where the radiation passes through the solar wind. In addition there is a slower modulation applied on top of this scintillation from drifting inhomogeneities in the Earth's ionosphere. This slower modulation is on the order of 30 seconds for each surge.

L-Bursts are generated at the top of the Jovian ionosphere at the foot of the tube of magnetic flux that passes through Io. The radiation is emitted in a hollow-cone beam with the axis of the cone tangent to the field line at the emission point.

We also observe S-Bursts which have individual durations of between 5-50 milliseconds. The S-Bursts drift higher in frequency at a rate of 20 MHz/sec. It is theorized that the source of S-Bursts is moving upward from the Jovian ionosphere in the magnetic flux tube that passes through Io and emitting radiation at the electron gyro frequency.

If we were able to receive the Jovian bursts before they passed through the solar wind or ionosphere they would consist of a series of repeated bursts, each of a approximately a minute in duration.

Table 3.2: Major Components of Jupiter’s Decametric Emissions above 15 MHz [5]

Source Designation	Range of System III CML	Range of Io Phase from SGC	Dominant Circular Polarization Component
Io A	200°-270°	205°-260°	RH
Io B	105°-185°	80°-110°	RH
Io C	300°-20°	225°-260°	LH at lower freq.
Non-Io A	230°-280°	Not dependent	RH

The average flux density of Jovian emissions is $5 \cdot 10^{-20}$ W/m²/Hz. During bursts though it is typically 10-20 dB greater. Using the antenna aperture computed in (3.1) we can determine that our antenna will see a power of between -98 and -88 dBm during bursts, which is detectable by our receiver.

CHAPTER 4

RECEIVER ARCHITECTURE

The greatest challenge for the receiver design was dealing with the many TV and radio transmitting stations located less than 10 km from our observing site (see Figure 4.1 which is a photo of one of the antennas with the TV broadcasting stations in the background). We measured FM broadcast stations at -9 dBm at the folded dipole antenna terminals ($1/8$ mW!). Four stages of filtering were necessary to prevent the amplifiers from saturating and to keep the FM broadcast band at an acceptable level.



Figure 4.1: This mountain is located about 2 km away from our observing site. The many TV and radio transmitters proved to be a significant hindrance.

The receiver consists of four basic elements: the antenna, low-noise amplifier, the power amplifier stage, and the digital receiver.

4.1 Antenna

Circumstances beyond our control forced us to place the first antennas close to the roof. Initially we chose to use a folded dipole architecture for our antenna as it offers a broad bandwidth and would be less affected by the proximity to the roof than other architectures [9]. The radiation pattern is shown in Figure 4.2. Simulation in 4nec2 indicated that the antenna input impedance was $450 + j379 \Omega$. We used a Coilcraft WB13-1TL RF transformer with a 13:1 impedance ratio to reduce this impedance to $36 + j29 \Omega$, a closer match to the 100Ω input impedance of our amplifiers.

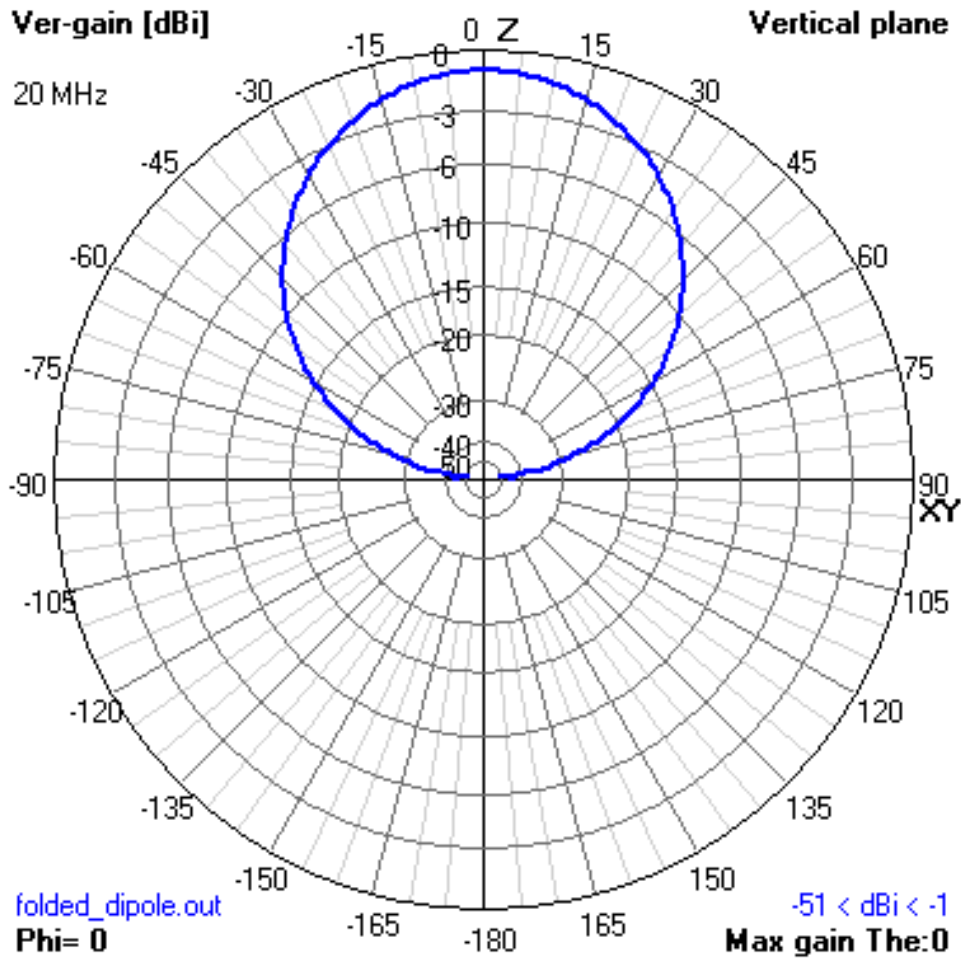


Figure 4.2: Folded dipole vertical radiation pattern from a simulation in 4nec2. The gain is measured in units of dBi, which is a measure of antenna directivity relative to an isotropic radiator (uniform radiation in all directions). It was not a very good antenna.

However later on we were able to switch to a $\lambda/2$ dipole architecture. We raised the antenna 5 1/4 feet (1.6 meters) above the ground and computed the pattern and S_{11} coefficient¹ in 4nec2 using 26 gauge copper wire. Each end of the antenna was 3.75 meters long. Figure 4.3 shows the pattern and Figure 4.4 shows a plot of the reflection coefficient versus frequency. The impedance at 20.1 MHz was $64 + j66 \Omega$.

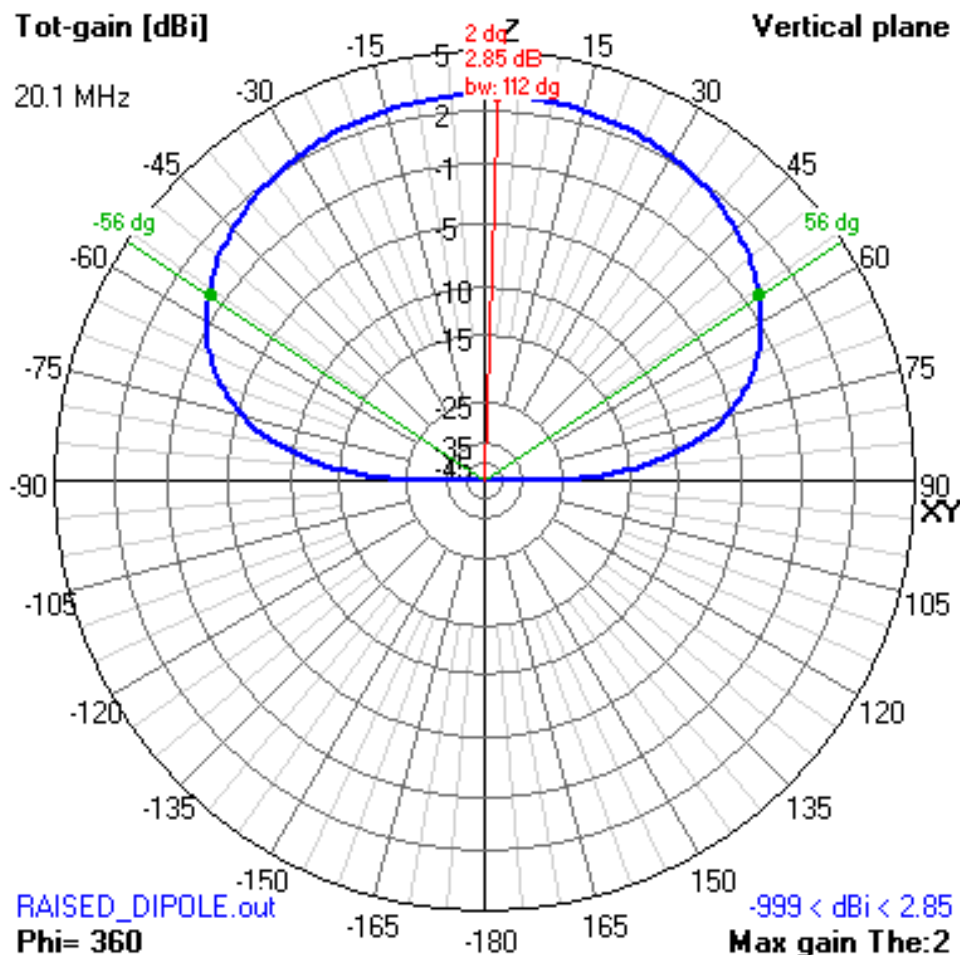


Figure 4.3: $\lambda/2$ dipole vertical radiation pattern. The gain is measured in units of dBi, which is a measure of antenna directivity relative to an isotropic radiator (uniform radiation in all directions). This antenna was a significant improvement on the earlier folded dipole.

¹ S_{11} is one of the “scattering-parameters” and is a measure of for a given input power how much of that power will be reflected back to the source. In terms of antennas S_{11} measures how good the antenna is at radiating power at a given frequency.

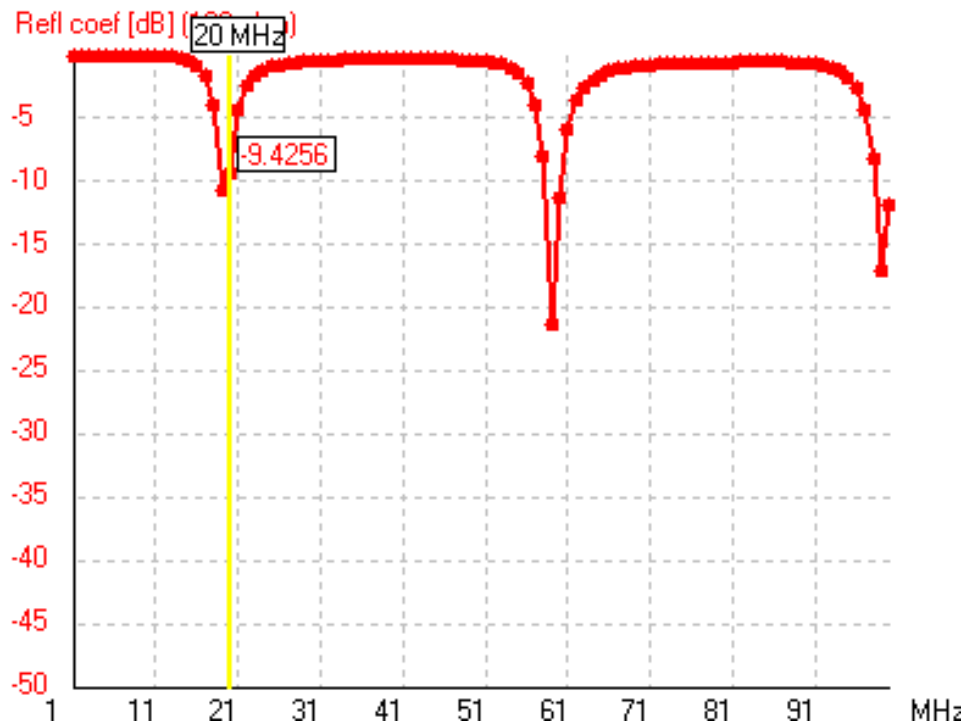


Figure 4.4: $\lambda/2$ dipole S_{11} . This plot shows the amount of power reflected back from the antenna versus frequency. Any power not reflected back is radiated by the antenna so low S_{11} is good.

4.2 LNA

The low-noise amplifier (LNA) is an “active balun”² design based on the work performed by Steve Ellingson [10]. The differential signal from the antenna is first low-pass filtered to reduce interferers and then amplified by two Mini-Circuits GALI-74+ amplifiers. The differential signal is then converted to single-ended by a Coilcraft WBC2-1TLB RF transformer. The LNA circuits only have two connections, one to the amplifiers and the second for the coax which carries both the RF signal and DC power. A bias tee splits the DC and RF at the receiver and at the LNA. Figure 4.5 shows a simplified schematic of the LNA. Note that the first transformer was present for the folded dipole but was removed for the half-wavelength dipole. The full schematic is shown in Figure B.1 and the bill of materials in Table B.1.

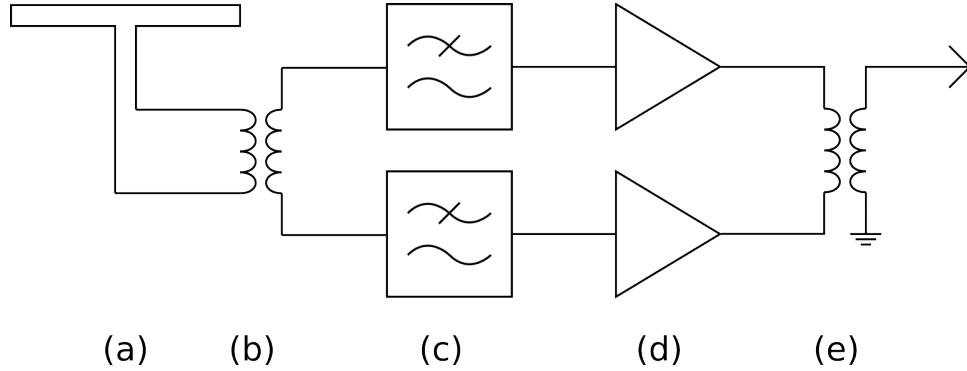


Figure 4.5: Simplified LNA schematic. The signal from the antenna (a) is first passed through a matching transformer (b) (this transformer was removed for the $\lambda/2$ dipole) and then each side is low-pass filtered (c) and amplified (d). Finally the signal is converted from balanced to unbalanced by a second transformer (e).

Initially we designed the LNA without the low-pass filters but this proved to be ill-advised. The signals from the TV and radio stations were so strong that they saturated the amplifiers. The addition of the low-pass filter before the LNA and

²A “balun” is a device that converts a balanced signal to unbalanced. A balanced signal is another term for a differential signal where a pair of wires carry two complementary signals. The signal is the difference between the two signals. Unbalanced is another term for single-ended where one wire carries the signal. The reference is typically ground. The output from a dipole is balanced but coaxial cable was designed to carry unbalanced signals, so we have to convert using a balun.

three bandpass filter stages on the power amplifier board reduced these interferers to an acceptable level with a nominal effect on the receiver noise figure. Figure 4.6 shows the S_{21} magnitude response³ of the LNA. A drawing of the LNA board is included in Appendix C and the PCB and Gerber files are included on the CD-ROM.

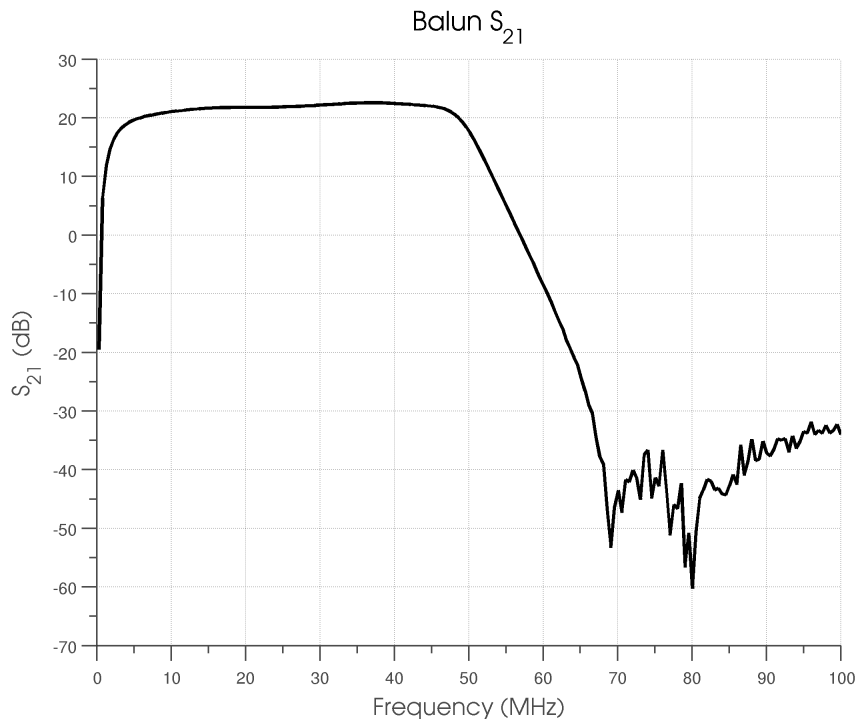


Figure 4.6: LNA S_{21} magnitude response. S_{21} is the forward transmission S-coefficient and is a measure of the gain of the LNA versus frequency.

The bias tee was installed in the penthouse⁴ to transmit power to the LNAs. A schematic is shown in Appendix B and a board drawing in Appendix C.

4.3 Amplifier Boards

The power amplifier stage has three stages of amplification, three bandpass filters per channel, and a variable attenuator to adjust the gain. Figure 4.7 shows a simplified schematic. The maximum gain is 65 dB with a -3 dB bandwidth of 2.5 MHz centered

³ S_{21} is another one of the “scattering-parameters” and measures how much gain (or loss) a device has at a given frequency.

⁴The “penthouse” is a small shack located on the roof of our physics building.

at 21 MHz. The minimum gain is 12 dB. The total gain in the FM band (88 - 108 MHz) is -56 dB at minimum attenuation. The control voltage for the attenuator is generated by a DAC which is controlled by the computer through an interface program running on an AVR microcontroller.

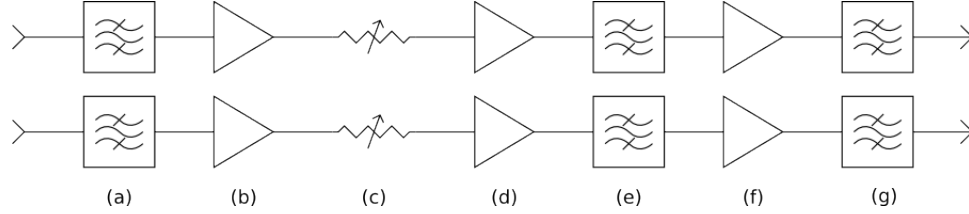


Figure 4.7: Simplified amplifier section schematic. There are two channels, one for each antenna. From the left the signals are first passed through a band-pass filter (a) and then amplified (b). Following the first amplifier is an adjustable attenuator (c) and two more sets of amplifiers (d), (f), and band-pass filters (e), (g).

Initially we put all three stages of amplification and both channels on the same board but we ran into problems with oscillation. We concluded that 70 dB of gain was simply too much and for the second revision of the amplifier board we only put two stages of amplification and one channel on each board. For the third stage of amplification we purchased a connectorized amplifier from Mini-Circuits. We also switched from a digital step attenuator to a voltage-variable attenuator at this point because of problems we had been having with the step attenuator not switching attenuation.

The new attenuator required 45 mA of current on the control line [11] so we were forced to buffer the low-power DAC with an op-amp in a voltage-follower configuration.

Unfortunately our network analyzer was out of commission when the board was finished, but Figure 4.8 shows the output intermodulation products. Figure 4.9 is a photograph of the completed amplifier assembly.

A complete schematic and bill of materials for the amplifier board is given in Appendix B. Note that C113, C114, and L103 and L104 are not included in the

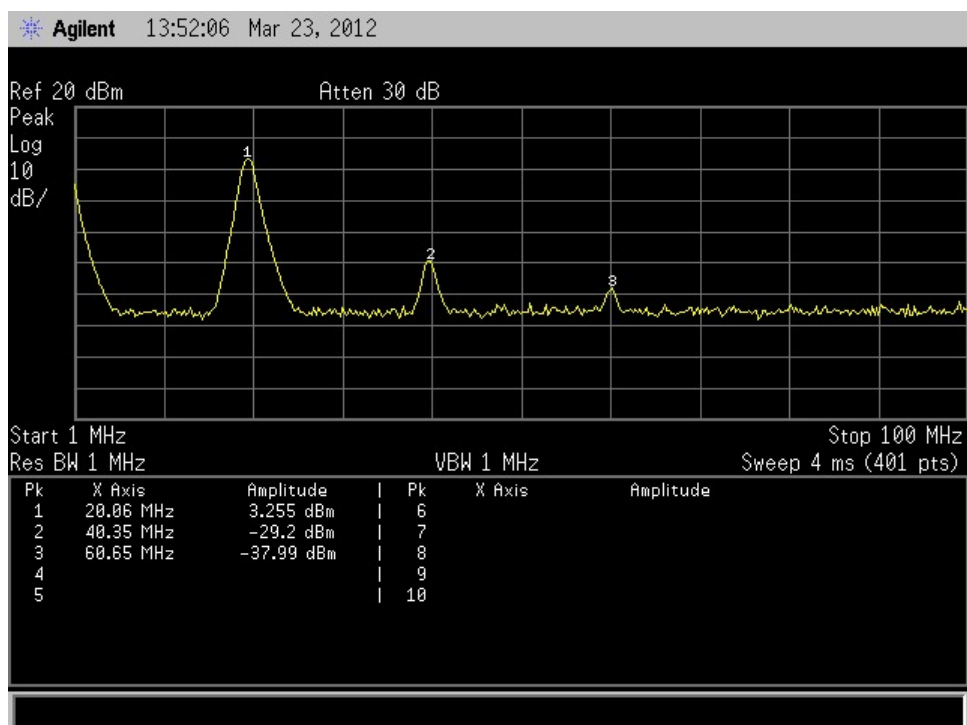


Figure 4.8: Amplifier board intermodulation products. All amplifiers have some non-linearities that generate signals at multiples of the input frequency. This plot shows the levels of these signals.

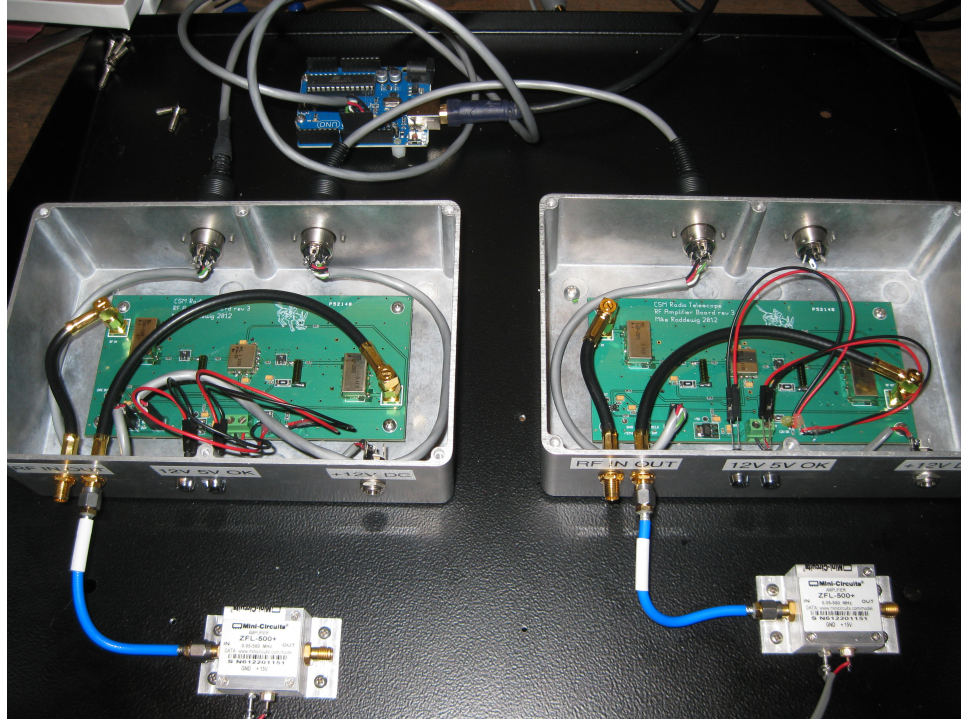


Figure 4.9: Photo of the amplifier assembly. At the rear of the shelf is the Arduino which controls the DACs. Mounted in front of it in boxes are the amplifier boards. Each board contains two sets of amplifiers and filters, the adjustable attenuator, and associated support circuitry. Two LEDs on the front indicate the status of the power supplies and a plug provides the 12 V DC input. The connectorized amplifiers on the front are connected after the amplifier boards and are followed by a pair of connectorized band-pass filters, one for each channel (not pictured).

board files. These were added to the design after the board was manufactured to knock out the high-frequency gain of the amplifiers and were hacked on to the board. A drawing of the board is included in Appendix C and the PCB and Gerber files are included on the CD-ROM.

4.4 ADCs and Software

The USRP contains the ADCs and a Xilinx Spartan-3A FPGA which performs the downconversion and filtering. The USRP reduces the initial sampling rate of 100 MSPS to 200 kSPS and downconverts the input signal to baseband. The USRP first downconverts the input signal using a CORDIC⁵ function and then reduces the sampling rate using a CIC filter followed by two halfband decimating FIR filters.

The reduced sampling rate data is then passed to the computer which performs the correlation and integration. The integration period is adjustable but was set at 0.5 seconds initially. The integrated samples are cataloged in files that are organized according to date and time. We use a Garmin GPS with a PPS output to synchronize the USRP to UTC time and each buffer of samples is individually time-stamped.

⁵COordinate Rotation DIgital Computer: a multiplier-less algorithm to calculate trigonometric functions, among other things. The USRP uses it as a downconverter.

CHAPTER 5

FABRICATION AND INSTALLATION

The telescope was installed on top of the roof of Meyer Hall. Most of the equipment was located in MH500 and the LNAs and antennas were placed at the far end to isolate them from the HVAC equipment as possible. We placed the LNAs close to the antennas to keep the noise figure low and to eliminate any degradation of the signal to noise ratio by the HVAC equipment after the LNAs. RG-58 was used for all RF interconnects as it is low-loss at 20 MHz and low-cost [12].

5.1 Folded Dipole Antennas

The folded dipoles were bolted to the sides of the roof apron so that they would not be visible from Guggenheim Hall. Two mounting brackets were fabricated and two porcelain standoffs were installed on each. The standoffs were installed with a spacing of 10 cm. The mounting brackets were fastened to the apron with masonry anchors (Figure 5.1). The distance between them was 7.5 meters. Pieces of irrigation tubing with slots cut in the end were used as spacers to hold the antenna wires apart and to form the feed line. Figure 5.2 shows a picture of the completed north antenna install.

5.2 Half-Wavelength Dipole Antennas

The half-wavelength dipoles were installed on 4x4 posts set into platforms that we placed cinder blocks on for stability. We stapled the ends of the wires to the outer 4x4s and screwed the LNA box into the center one. No matching transformer was needed for the new configuration. The end 4x4s were 7.25 meters apart and the wires were stapled to the 4x4s so that they were approximately 1.6 meters off the ground. Figure 5.3 shows the completed north antenna. The old folded dipole

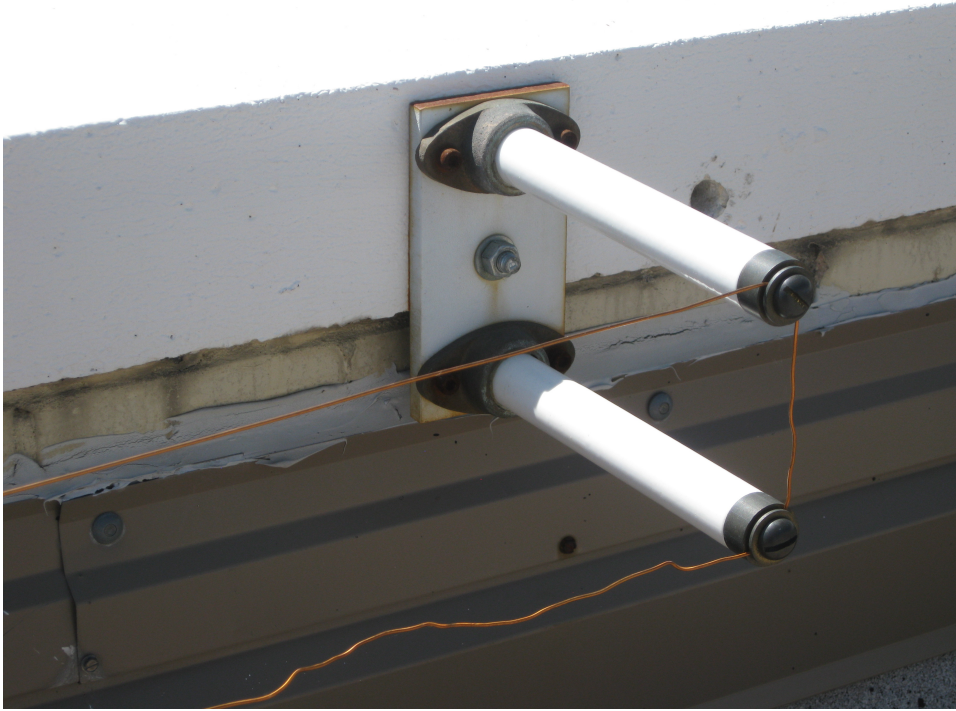


Figure 5.1: One of the folded dipole antenna mounting brackets, photographed while the antenna was still in service.

mounting brackets are visible in the background. The LNA was screwed into the center 4x4 (Figure 5.4). The center ends of the dipole wires were attached to the terminal posts without any extra hardware. The antennas were again placed in a north-south configuration. The new baseline is slightly smaller than the old baseline at roughly 17 meters but the 17 meter fringe pattern shown in Figure 5.5 shows little difference from the old 18 meter fringe pattern in Figure 2.2.

5.3 LNAs

The LNA boards were fabricated on 60 mil FR-4 substrate and assembled in our lab. They were installed in custom-machined weather-proof boxes and fastened to the roof apron using masonry anchors. The RF and DC connector is an N-type and the antenna connector is a standard terminal jack. Unfortunately the weather-proofing on the boxes was inadequate so when we upgraded the LNAs to a new design the



Figure 5.2: Picture of the completed north folded dipole antenna install. The antenna is difficult to see but it follows the wall. The conduit on the right contains the coax that is connected to the LNA which is bolted to the wall.



Figure 5.3: The northern half-wavelength dipole. The 4x4 are weighted with cinder blocks to prevent them from blowing over. The antenna wires are very difficult to see but they are stretched between the 4x4s. The LNA is attached to the top of the middle 4x4.

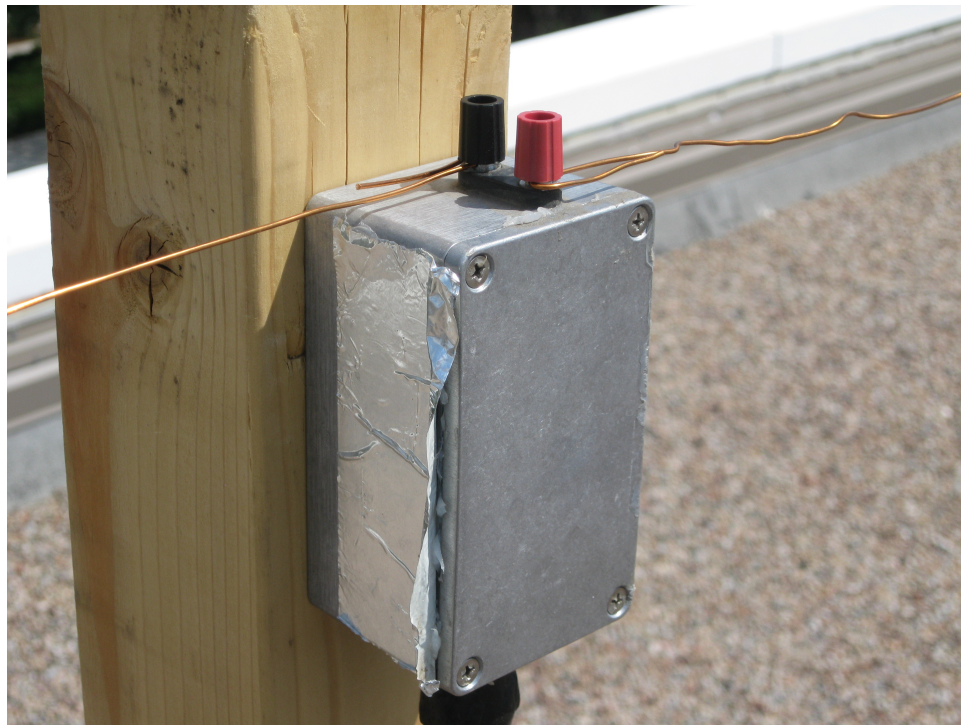


Figure 5.4: The northern half-wavelength dipole LNA, attached to the middle 4x4. The antenna wires are simply fed through the terminal posts and then looped around. The entire assembly is generously sealed with silicone.

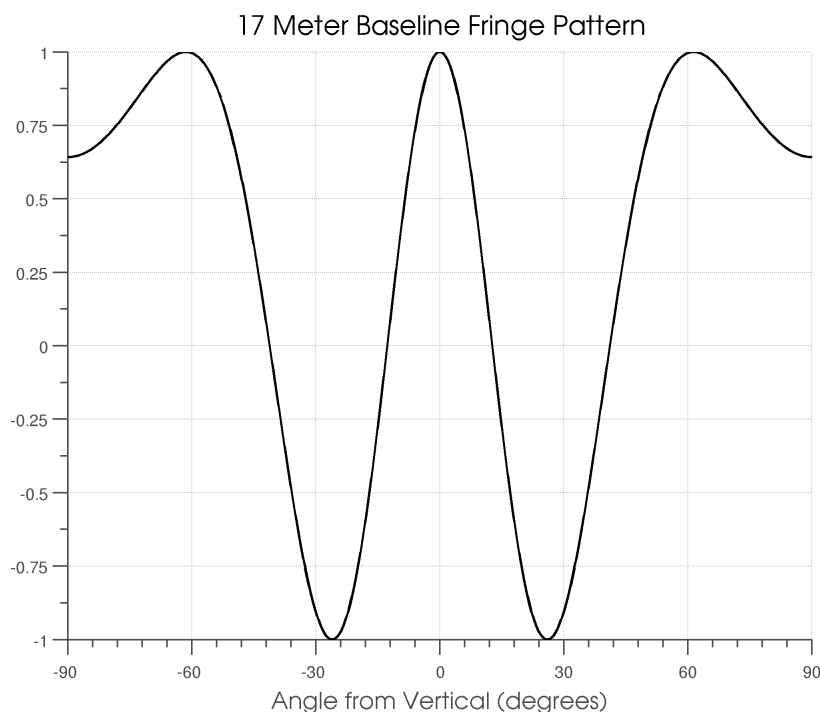


Figure 5.5: Interferogram with the new $\lambda/2$ dipole 17 meter baseline. No change is evident from the old 18 meter baseline.

boxes were sealed with silicone sealant and the tops taped with foil tape to keep water out. The RF connector is protected with Coax-Seal. Figure 5.6 shows the north LNA box and Figure 5.7 shows the LNA board installed inside the box. The matching transformer was a late upgrade and was installed between the LNA and antenna. Wires were soldered to the transformer leads and then the entire assembly was submerged in marine epoxy (Figure 5.8).

For the half-wavelength antennas we fastened the LNA boxes to a 4x4 in the middle. We connected the antenna leads directly to the terminal posts on the LNA.

5.4 Lightning Protection

A big concern was how to handle a lightning strike on one of the antennas. Fortunately the amateur radio community has produced several articles that serve as an excellent tutorial on lightning protection [13].



Figure 5.6: Picture of the north LNA box as it was installed for the folded-dipoles.

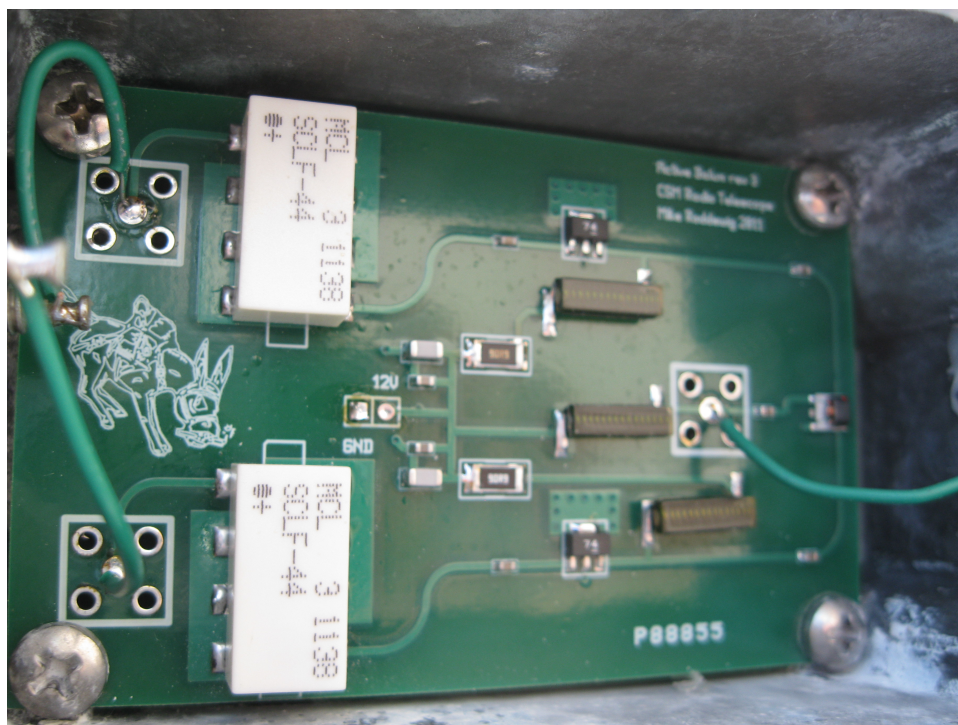


Figure 5.7: Picture of the north LNA board installed inside its box. The mineral scale on the walls of the box is from an old water leak that we fixed.

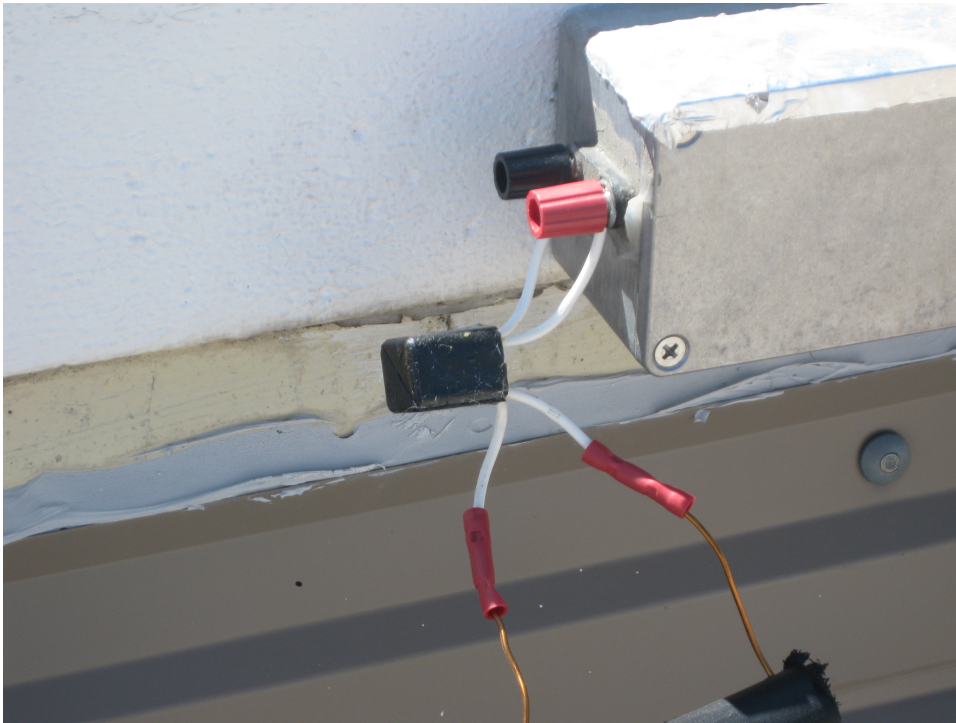


Figure 5.8: The external matching transformer for the folded-dipole antennas. This was an after-thought so it was installed outside of the LNA box. We soldered wires to the transformer leads and then submerged it in marine epoxy to weatherproof it.

We installed a large copper panel to act as a ground panel and surge suppressors for all connections that are made to the telescope: power (PolyPhaser PLDO-120US15A), antennas (HyperLink AL6), Ethernet (PolyPhaser IXG-05), and GPS (PolyPhaser IX-6L). Each of these surge protectors was mounted to the panel.

Two ground straps were mounted to the panel as well. One was used to connect the equipment rack to the ground panel, the other was used to connect the ground panel to a low-impedance ground. The best low-impedance ground turned out to be a disused well located in a service tunnel beneath Meyer Hall. Luck would have it that a ventilation shaft that ran from the penthouse to the second floor was directly above this service tunnel so we had a hole drilled for our ground strap and then ran it all the way from the ground panel into the well beneath Meyer.

Figure 5.9 shows the installed ground panel. From left to right there are surge protectors for data (GPS), Ethernet, two coaxial surge protectors for the RF connections, and power.

Unfortunately we were not able to ground the antennas or LNAs. In the event of a lightning hit the energy would be directed along the coaxial cable where the ground panel would short it to ground. During this event the antennas and LNAs may be damaged or destroyed. There was no financially feasible way to prevent this so it is simply a limitation of the system. However the system should prevent any damage to the power amplifiers, USRP, computer and related equipment. It will also diminish the possibility of a fire in the penthouse.

5.5 Computer, USRP, and Amplifier Board

We decided early on to make the indoor equipment rack-mount for easy maintenance and organization.

The computer is an Intel Atom device with two cores that run at 1.6 GHz and it has two Seagate Constellation 1 TB hard drives configured in a RAID 1 array. The motherboard has two gigabit Ethernet ports, one of which is connected to the campus



Figure 5.9: Picture of the copper ground panel. From left to right are the GPS and Ethernet surge protectors, the coaxial surge protectors, and the AC surge protector. These are all bolted to the copper ground panel. At the bottom are two ground straps, the left leads to the equipment rack and the right travels down five stories to the well in the basement of our building.

network and the other to an internal switch which connects the USRP and a remote power switch to the computer. The computer case is mounted on slides so that it can be pulled out for easy maintenance.

The computer runs Scientific Linux 6 which is based off of Red-Hat Enterprise Linux. It is designed to be headless and all administration can be performed via SSH or, if the computer is having network problems, a local serial console running at 38400 8N1. The BIOS and GRUB are both set up to be accessed from the serial console. A USB to serial converter is hooked to the computer so a laptop can be connected to the serial console for administration.

An APC Smart-UPS SC 450 uninterruptible power supply (UPS) ensures that the telescope will continue to operate during power outages and provides power to the computer and the RF hardware. The computer communicates with the UPS via serial and `apcupsd`. AC power from the UPS is distributed using a Tripp-Lite power-distribution unit.

A Furman power conditioner conditions the AC power that is input to the UPS. We had a power outage that destroyed the UPS so I installed the power conditioner to hopefully prevent that from happening to its replacement.

The remote power switch is a SynAccess netBooter np-02 and controls the power to the USRP. The USRP needs to be power-cycled after every firmware or FPGA update so the power switch allows for remote development. It is configured to use an IP address of 192.168.10.100 and the default username and password of “admin” and “admin”. The USRP is connected to the first AC port.

The USRP is connected to the internal gigabit switch and given the default IP address of 192.168.10.2 and named “genesis”.

The internal network is accessible via an OpenVPN server installed on the computer.

Environmental monitoring is provided by a 1-Wire temperature and humidity sensor. MUNIN is used to aggregate and graph the cabinet temperature and humidity as well as many other system parameters and automatically emails alerts when parameters exceed set-points.

The amplifier board attenuator microcontroller is connected to the computer via USB and appears as `/dev/ttyACM0`. It mimics a serial port running at 38400 8N1.

A 12V linear power supply provides power for the amplifiers, balun, and GPS. It is fused with a 1.5A fuse to provide protection in the event of a short-circuit or equipment failure. A voltage gauge displays the voltage on the 12V bus and a pair of banana terminals allow a multimeter or other equipment to be connected to it. The current gauge displays the current consumption of the balun and the switch at the top of the rack powers the balun off and on.

Figure 5.10 shows the equipment rack and Figure 5.11 shows the rack and ground panel as they were installed in the penthouse.

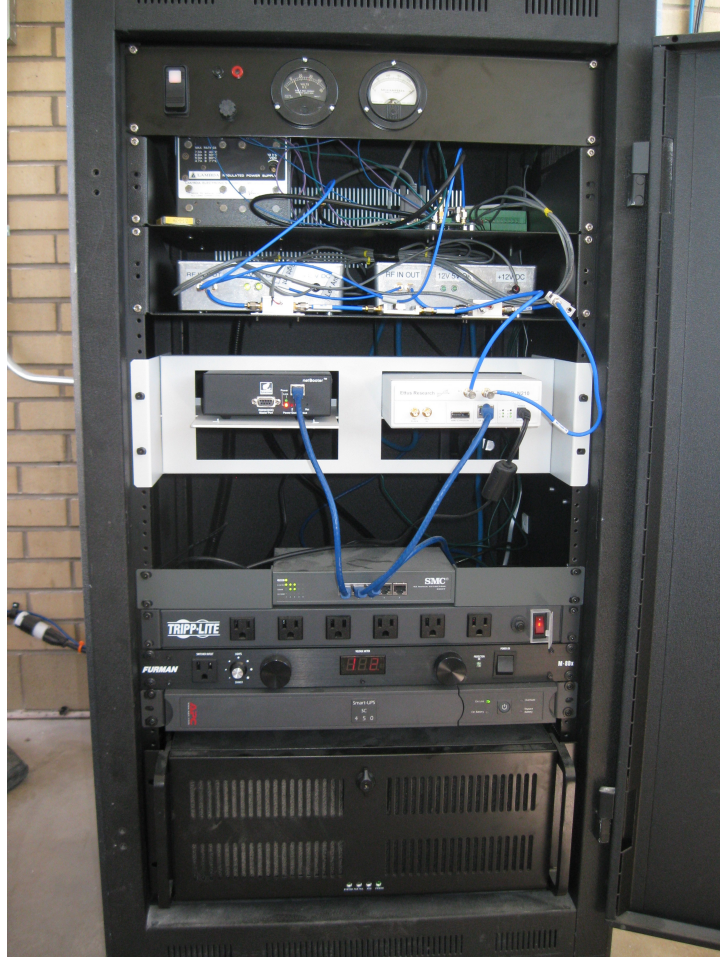


Figure 5.10: Picture of the equipment rack. At the top is a panel with a switch to power off the LNAs, a voltage meter connected to the 12 V bus, and a current gauge that monitors the current that the LNAs are drawing. Below them on the first shelf is the 12 V linear power supply, the bias tee board, and 12 V and ground screw terminal assembly. The next shelf down contains the amplifier assemblies. Below that is the USRP and a remote power switch which controls the power to the USRP. Both the USRP and remote power switch are connected to a network switch which is on the internal network for the telescope. Below the switch are the power-distribution unit, a power conditioner, and the UPS, and at the bottom is the computer.



Figure 5.11: The penthouse equipment room. The grate in the lower right-hand corner leads to a service tunnel underneath the building where we grounded the system. The sign warns that no conductive materials should be placed within 48 inches of the rack or ground panel to reduce the possibility of lightning arcing over and escaping our containment system.

CHAPTER 6

SOFTWARE

The software was written in C for the Linux operating system. Its function is to receive the samples from the USRP, correlate and integrate them, and then catalog them according to date. There are two basic programs, `telescope_usrpd` and `telescope_sqld`. The programs communicate with each other through standard C streams using a data structure, `telescope_message_header_t`, shown in Listing 6.1. `telescope_message_header_t` prefaces the message and specifies the number of samples that follow, the time that they were taken using `record_time` which contains the year, month, day, hour, minute, and whole seconds, `fractional_secs` which contains the fractional seconds, and a `flags` byte that is used to indicate an error upstream. No checksum is used but each program checks that the number of samples that follow is the same as was specified in the message header. The init script included with the software sets up a FIFO to send the output from `telescope_usrpd` to `telescope_sqld`.

Listing 6.1: `telescope_message_header_t`

```
typedef struct {  
    tm record_time;  
    double fractional_secs;  
    int32_t num_samples;  
    uint8_t flags;  
} telescope_message_header_t;
```

6.1 `telescope_usrpd`

`telescope_usrpd` initializes the USRP, receives the data and correlates and integrates it. Figure 6.1 shows the basic signal-processing operations that take place. The signals from both channels are scaled using a constant scaling gain $g = 10^6$ and

then cross-correlated and integrated. The magnitude-squared power for each channel is also computed individually. The integration is performed using the trapezoidal method and the default integration period is 500 milliseconds, although depending on the buffer size and USRP sample-rate the software may not be able to achieve that exactly. After integration the magnitude of each sample is taken and the result is passed to `telescope_sqld` for storage.

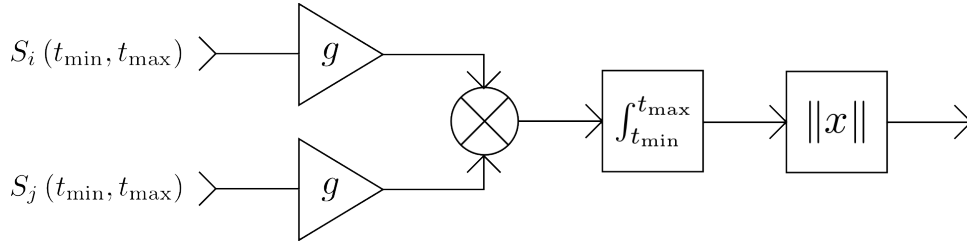


Figure 6.1: The signal processing operations performed by the software. The multiplication is of the form $S_i \cdot S_j^*$. i and j are the channel being processed, so there are three separate signal-processing channels. The first two channels compute the power of each channel with $i = j = 1$ and $i = j = 2$. Because the channel is multiplied with its conjugate the two-norm at the end is redundant, but is used in the software to convert the `complex` type to a `double`. For the final channel we multiply $i = 1, j = 2$ which is the cross-correlation at zero-lag. In this case the result is not necessarily real so we take the two norm to compute the magnitude. In general the integrator period $t_{\max} - t_{\min}$ is 500 milliseconds but can be altered on start-up.

`telescope_usrpd` has a number of different options that are specified on start-up. The sample rate, receive frequency, integration period, and USRP gain are all customizable by the user.

Source code for `telescope_usrpd` is included on the CD-ROM.

6.2 telescope_sqld

`telescope_sqld` collects the samples from `telescope_usrpd` and stores them in a SQLite3 database. Each sample is stored with the time it was taken in Julian date format in the `data` table. The `data` table contains the following columns:

- `date` contains the Julian date on which the sample was taken

- `cross` contains the cross-correlated sample
- `auto1` contains the power sample for channel 1
- `auto2` contains the power sample for channel 2
- `config_id` contains the primary key of the configuration that was used to take this sample stored in the `config` table

The `config` table contains the following columns:

- `period` contains the integrator period in seconds
- `gain` contains the USRP gain in dB
- `rxfreq` contains the USRP receive frequency in Hz
- `samplerate` contains the USRP sample rate in samples/second
- `cross_a` contains the constant a for the cross channel calibration
- `cross_b` contains the constant b for the cross channel calibration
- `auto1_a` contains the constant a for the channel 1 calibration
- `auto1_b` contains the constant b for the channel 1 calibration
- `auto2_a` contains the constant a for the channel 2 calibration
- `auto2_b` contains the constant b for the channel 2 calibration

The calibration function is a first-order polynomial of the form $f(x) = ax + b$ that converts the output of the receiver into units of electric field flux in Jansky ($1 \text{ Jy} \triangleq 10^{-26} \text{ W/m}^2/\text{Hz}$). The constants are passed to `telescope_sqld` on startup via command-line options.

In the event of an overflow (indicated by the upstream process setting a flag in the `flags` byte of `telescope_message_header_t`) `telescope_sqld` simply ignores that sample and continues inserting samples with the next non-error sample.

6.3 Attenuator Controller

The software to control the attenuator runs on an Arduino Uno which contains an AVR ATmega328 microcontroller. This microcontroller has a Serial Peripheral Interface (SPI) which is connected to the amplifier boards to control the DAC. The program communicates with the computer over a USB bus where it mimics a serial terminal running at 38400 8N1. On startup the program outputs “SPI Controller v1.0” and provides a simple command prompt. It accepts 24-bit lower-case hexadecimal values in the form 0xxxxxxx which it transmits on the SPI bus. If the command syntax is correct it prints out the transmitted value. If the command syntax is incorrect it prints “Invalid command”. A sample interaction is given in Listing 6.2.

Listing 6.2: AVR Attenuator Controller Sample Interaction

```
SPI Controller v1.0
> 0x00ffff
Transmitted 0x00FFFF
> 0x003fff
Transmitted 0x003FFF
> 0xX
Invalid command
>
```

The program is written in C for the avr-gcc compiler and uses functions from avr-libc. Source code is included on the CD-ROM.

CHAPTER 7

RESULTS

A big impediment that I did not foresee was the broadband noise that was emitted by the HVAC equipment that was on the roof of our building (see Figure 7.4). Because this noise is broadband it is impossible to remove by filtering and effectively “drowns out” many solar emissions. But I am still able to discern stronger bursts. I am hopeful that the performance of the telescope will improve in winter when the exhaust fans have been turned off.

7.1 Receiver Performance

Using formulae given in [14] I predicted the cumulative noise figure of the receiver to be 3.387 dB.

Calibration revealed the sensitivity of the first channel to be -104 dBm (Figure 7.1) and the second to be -114 dBm (Figure 7.2, I tested in 10 dB steps). I am not sure why the channels behave differently, ideally they should both be exactly the same. Unfortunately I did not have time to troubleshoot the problem, but the telescope continues to function even with this discrepancy.

I used a signal generator inject an AWGN signal into each channel. In the plots the signal generator is turned at -114 dBm at about sample 30 and then stepped to -104 dBm at approximately sample 400.

The antennas were calibrated using a first-order polynomial function to map the integrator outputs to power in Jansky ($1 \text{ Jy} \triangleq 10^{-26} \text{ W/m}^2/\text{Hz}$). The receiver was calibrated at four power settings: -114 , -104 , -94 , and -84 dBm. Because the northern receiver was not as sensitive as the southern receiver I only used the last three values to perform the calibration. Using MATLAB’s `cftool` a first-order polynomial of the form $f(x) = ax + b$ was fitted to the data.

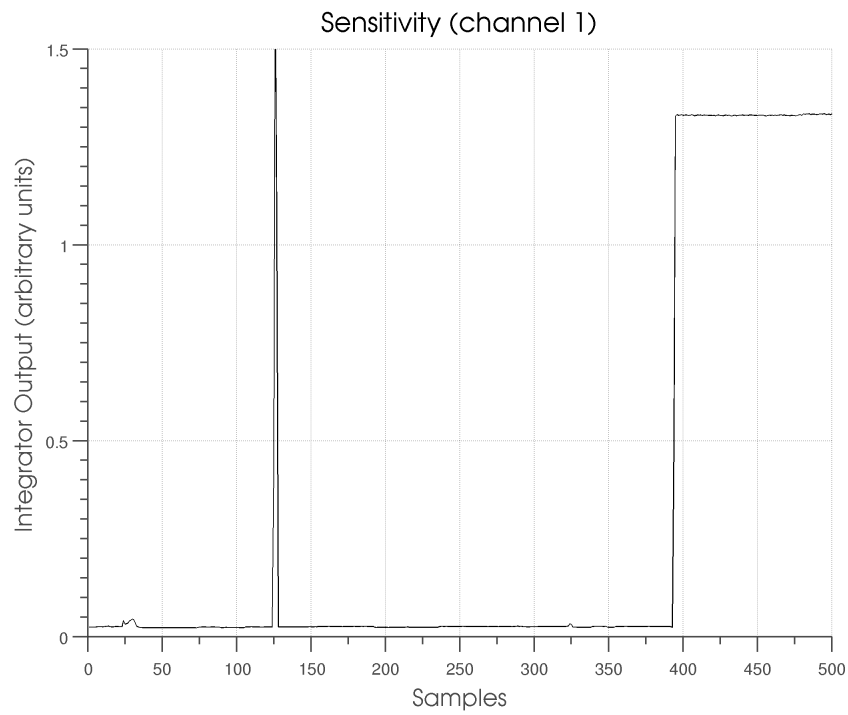


Figure 7.1: Channel 1 sensitivity testing and calibration. The signal generator was turned on at sample 30 with a power of -114 dBm and we increased the input power by 10 dB at sample 400.

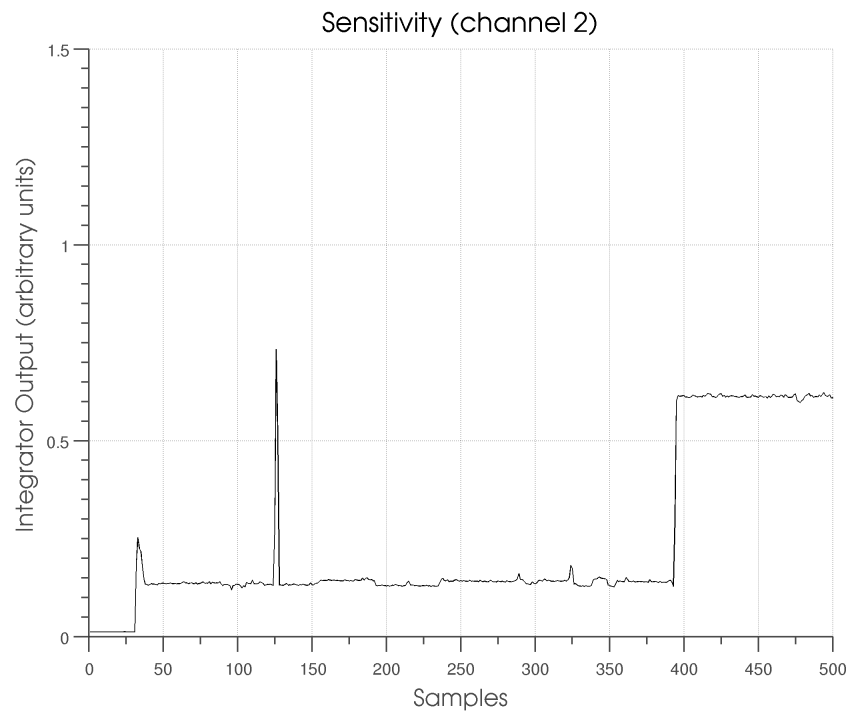


Figure 7.2: Channel 2 sensitivity testing and calibration. The signal generator was turned on at sample 30 with a power of -114 dBm and we increased the input power by 10 dB at sample 400.

At this point I made a compromise. I was fitting a linear mapping function but the amplifiers do not have a linear response at the upper and lower boundaries of their transfer function. The calibration was only valid between approximately $400 \cdot 10^3$ Jy and $23.5 \cdot 10^6$ Jy. Above and below these points the error between the interpolated power from the mapping function and the actual input power would begin to grow quite large. Because of this the quiescent output values of the calibration function tended to be much lower than the actual noise floor of the amplifier. To remedy this I fixed a lower boundary for the b constant at $2.579 \cdot 10^5$ Jy to keep the error at low output values from growing too large. This slightly increased the root-mean-square error (RMSE). Table 7.1 shows the computed constants and the RMSE.

Ideally we would use a third-order polynomial of the form $f(x) = ax^3 + bx^2 + cx + d$ which would be able to accurately reproduce the non-linearities at the boundaries of the amplifiers' responses, but I did not have time to upgrade the software again to support such a change.

Table 7.1: Calibration constants a and b to convert the receiver output to units of flux in Jy. The calibration function is of the form $f(x) = ax + b$.

	a	b	RMSE
Channel 1	$2.708 \cdot 10^4$	$2.579 \cdot 10^5$	$3.96 \cdot 10^5$
Channel 2	$5.032 \cdot 10^4$	$2.579 \cdot 10^5$	$6.62 \cdot 10^4$
Cross-Correlation	$3.729 \cdot 10^4$	$2.579 \cdot 10^5$	$3.33 \cdot 10^5$

I also tested the phase match between the antennas. Initial testing revealed a 3 ns difference between the antennas. I cut a 1 meter long piece of piece of coax and inserted it to match the two antennas. Figure 7.3 shows the result as measured on our oscilloscope. The final phase difference was measured to be 1 ns which equates to an offset of 1° .

The gain of a single channel was calculated to be 78 dB, which is close to the predicted value of 78.87 dB.

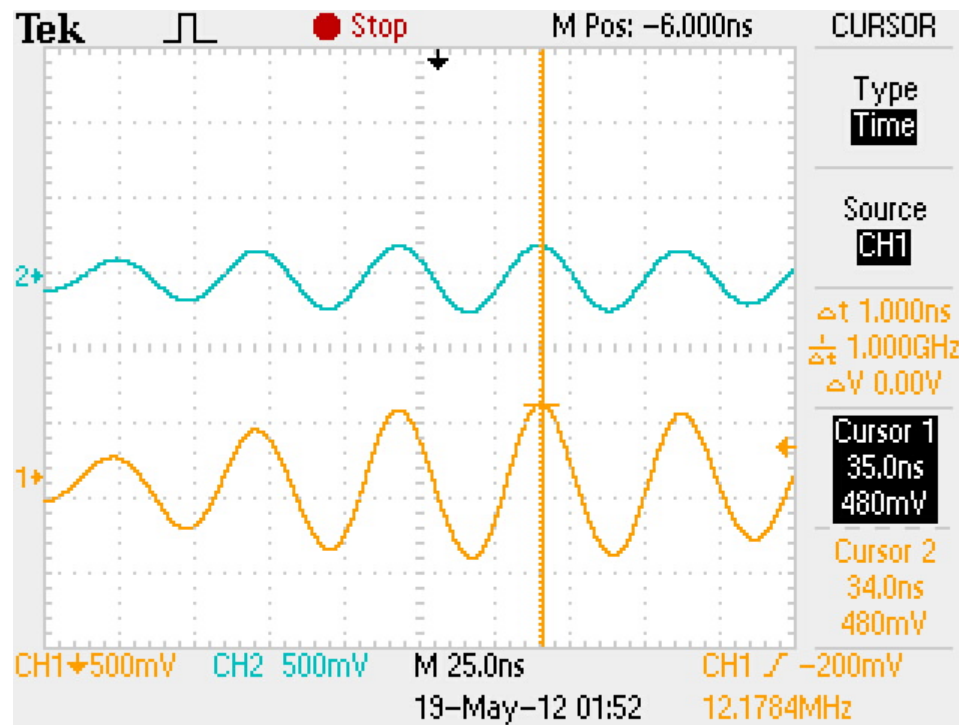


Figure 7.3: Phase match testing using an oscilloscope. Channel 1 is attached to the output from the receiver for the north channel and channel 2 is attached to the output from south channel. By comparing the phase of both signals we were able to determine how closely phase-matched each channel was.

7.2 HVAC Noise



Figure 7.4: Our antennas are located very close to the noisy HVAC equipment. The many AC induction motors in the background contributed significant RF noise to the system.

To quantitatively show that the roof was electrically noisy I built a “coax probe” antenna that I attached to our handheld analyzer. The probe was simply a 3 foot length of RG-58 with the shield removed. Figure 7.5 shows the S_{11} parameters of the antenna. It is a rather poor antenna at 20.1 MHz but sufficient for our purposes. Figure 7.6 shows a spectrum taken next to the northern antenna while Figure 7.7 shows a spectrum taken in the Patridge Park parking lot north of Golden (a relatively radio-quiet area for comparison). The power measured on the roof was -138 dBm while the power measured at the Leyden Road site was -150 dBm (both in a 1 Hz bandwidth). I also took a measurement in the middle of Kafadar Commons which is shown in Figure 7.8.

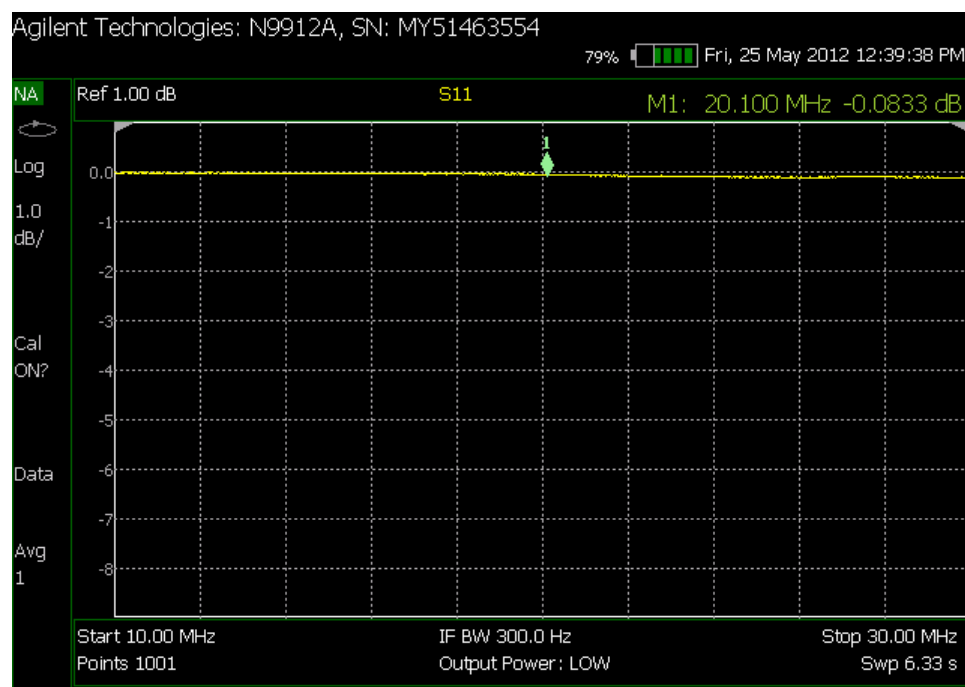


Figure 7.5: Coax probe S_{11} , detailing the poor performance at 20.1 MHz of the coax probe used to test for noisy equipment near our antennas.

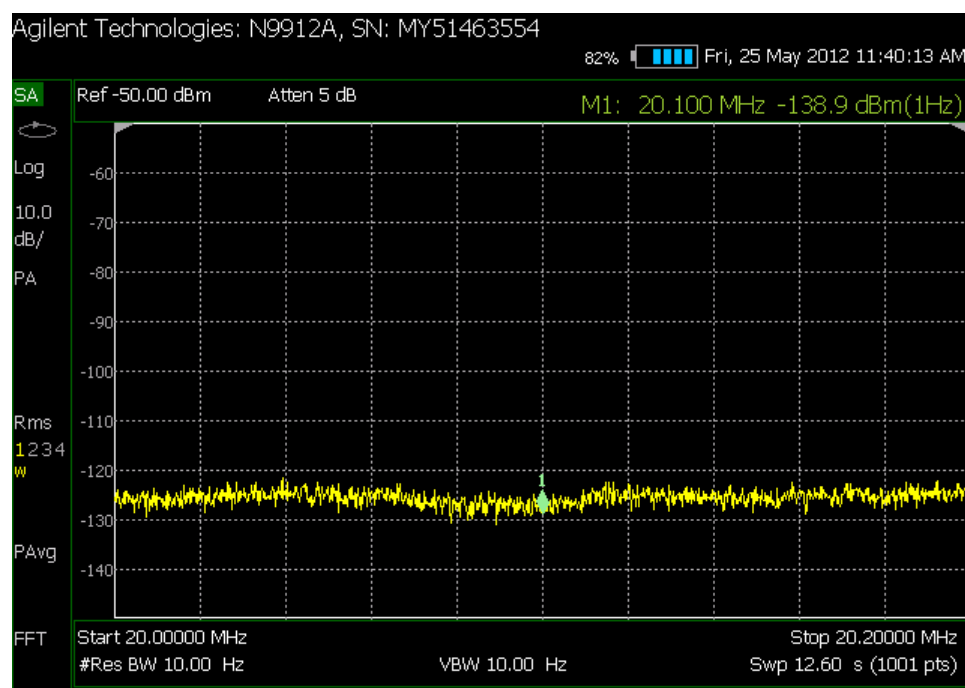


Figure 7.6: Spectrum taken next to the northern antenna using the coax probe. The marker located at 20.1 MHz shows the power in a 1 Hz bandwidth.

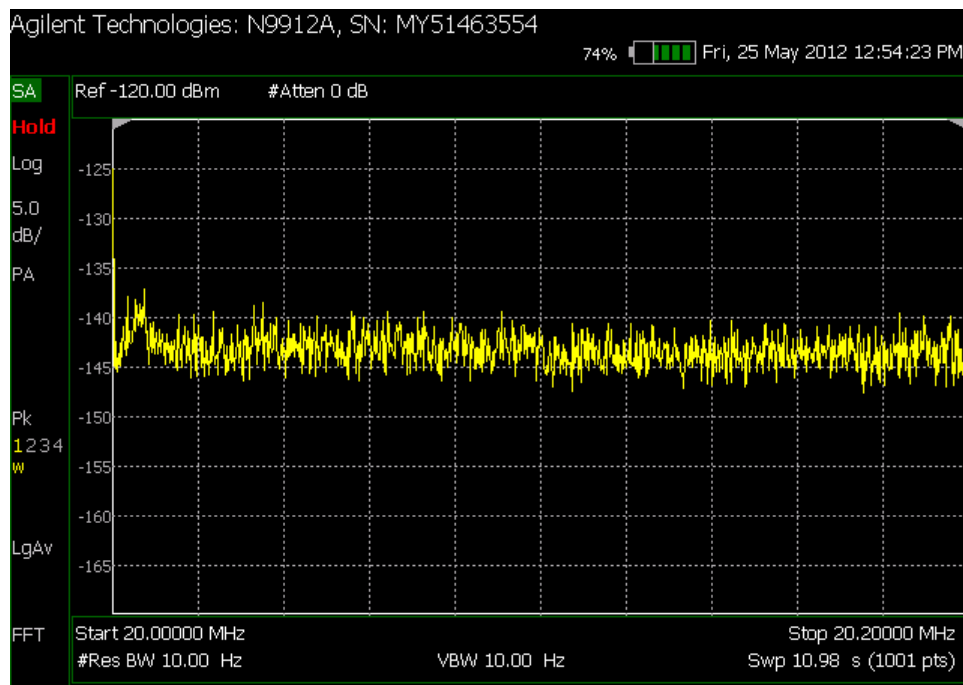


Figure 7.7: Spectrum taken in the Pattridge Park parking lot using the coax probe. The marker located at 20.1 MHz shows the power in a 1 Hz bandwidth. I considered this to be an electrically “quiet” area to use as a comparison to roof where the antennas are located.

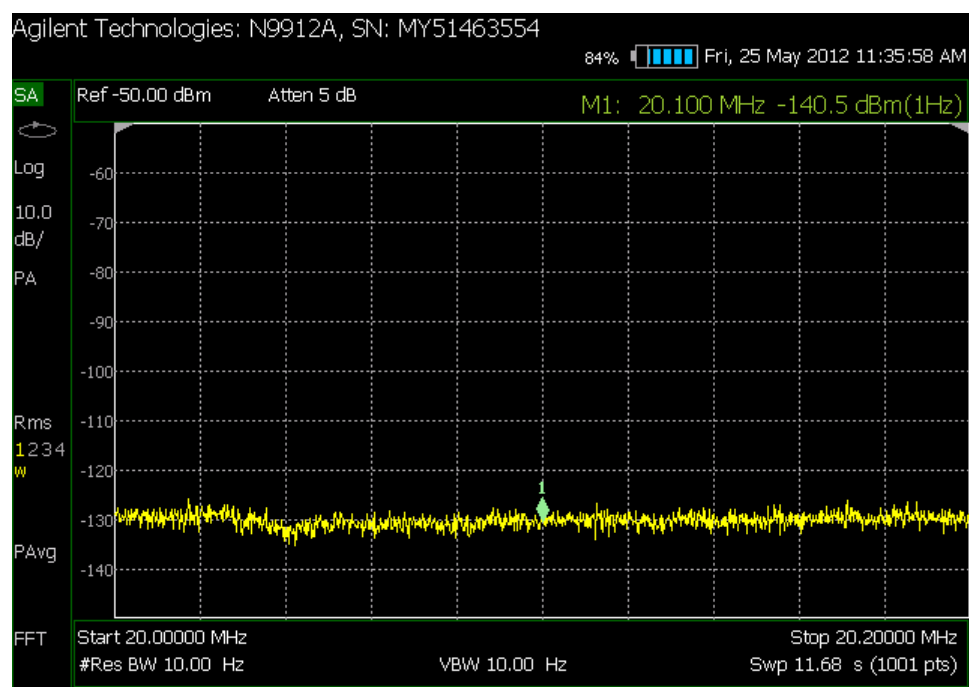


Figure 7.8: Spectrum taken using the coax probe in the middle of Kafadar Commons, a parade field located next to our physics building. This was to see how electrically quiet the campus was in general.

The culprits appear to be the numerous exhaust fans (see Figure 7.9 for an example) located on the roof of Meyer Hall. Figure 7.10 shows a spectrum taken next to one such fan. The noise power at 20.1 MHz is -130 dBm. Curiously the fume hood vents were electrically quiet. I postulate that this is because all of their vents are screened.

I also noted a periodic nature to the noise, as shown in Figure 7.11⁶. The noise would turn on abruptly each morning at 7:30 AM and off each evening at 7:30 PM. This seems to indicate that the noise is of a man-made nature as opposed to be a natural process.

Since the LNAs are encased in waterproof boxes I thought that the noise might be caused by heating of the amplifiers but I dismissed this theory because it would

⁶Note that the integrator units in this figure are not comparable to those in Section 7.3. This plot was taken before the receiver settings were finalized.



Figure 7.9: One of the strong RF noise emitters is this exhaust fan, approximately 10 meters from the north antenna.

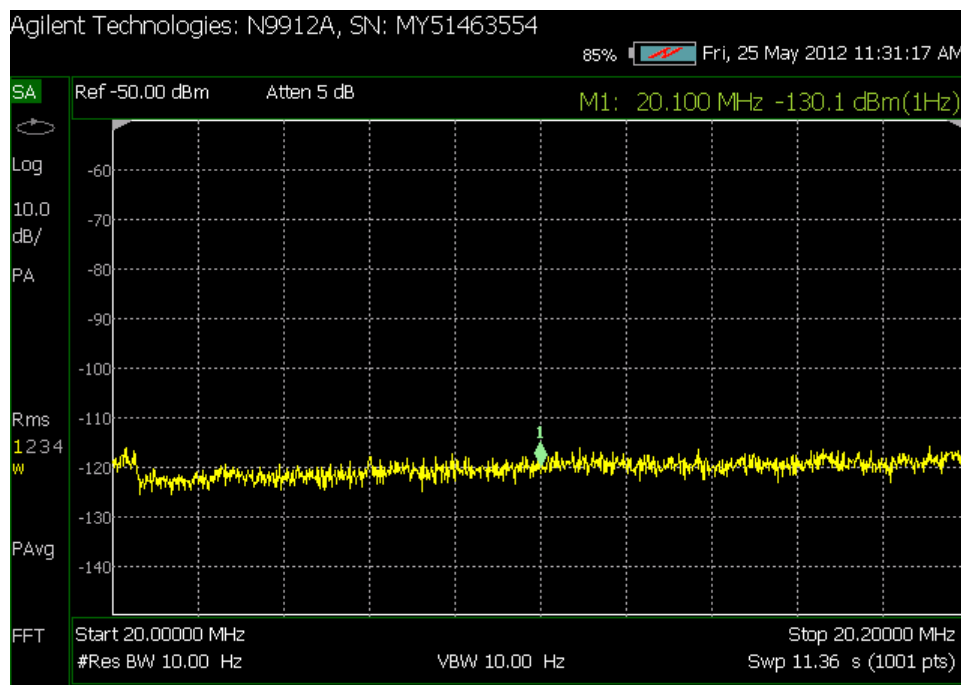


Figure 7.10: Spectrum taken using the coax probe next to the exhaust fan shown in the previous figure.

not be an abrupt change like I was seeing. It would make sense that the noise was coming from the exhaust fans because they would only run during the day when the building was hot. Additionally when there was a very hot day the noise would not turn off in the evening presumably because the fans would run all night.

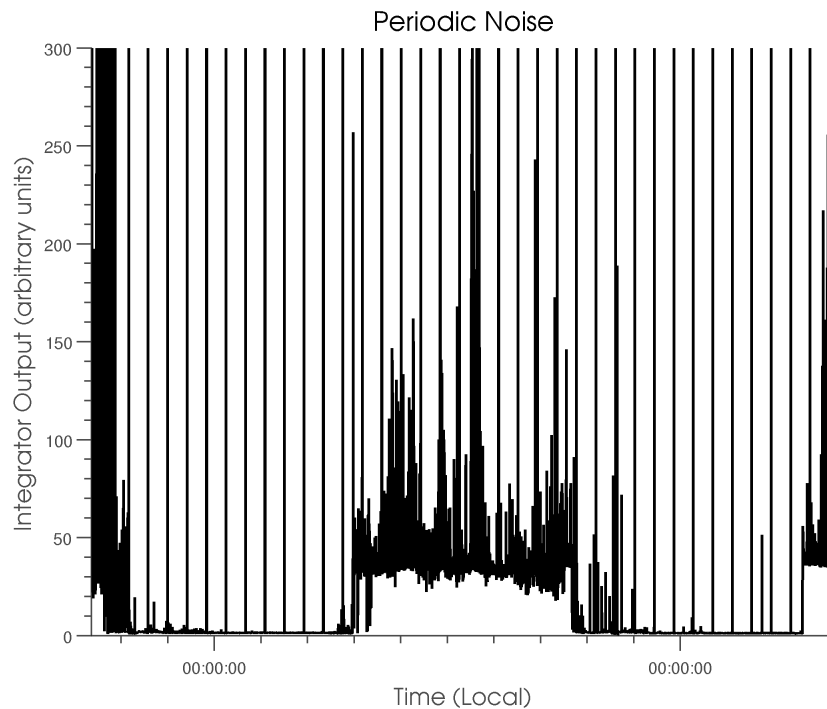


Figure 7.11: Interferometer output over an approximately 30 hour period. During this part of the year we believe the exhaust fans were being turned off at night, hence the abrupt, periodic drop in the background noise seen by the receiver.

The noise was periodic for a time but as we moved further into summer (and the outdoor temperature increased) it became constant, again I theorized this was because the exhaust fans were no longer being turned off at night.

To confirm the source of the noise I performed several tests. I thought it was possible that the noise might be entering the system through the AC circuit. Testing this theory was simple because the telescope runs on a UPS. I simply unplugged the telescope from the AC hard-line. When I did this there was no change in the noise power.

To check that the noise was not coming from inside the rack of the telescope I disconnected the coax lines where they entered the penthouse and terminated the lines going to the amplifiers. There was a significant drop in the noise power so this indicated that the noise was coming from outside of the penthouse.

I then checked to see what the result of powering off the LNAs was. There was again a significant drop in the noise power which indicates that the noise is entering the system before the LNAs, either at the antenna terminals or at the antenna itself.

These results seem to confirm that the noise is from an external man-made source.

7.3 Solar Bursts

We upgraded the software twice in the course of recording data. The first upgrade we made was to support calibration of the receiver so we could relate the receiver output and the flux of the wave striking the antenna and to store the flux densities seen at both channels in addition to the cross-correlation. The second upgrade was to switch the software to use complex-valued data instead of immediately converting the complex samples from the USRP into real values and correlating those. All of the following bursts were taken before either upgrade was made. Figure 7.25 was taken after the first upgrade to support calibration but before we switched to complex data. Figure 7.23 and Figure 7.24 were both recorded after all upgrades had been completed.

Figure 7.12 shows a solar burst captured on June 14, 2012 at 21:38:20 UTC. Figure 7.13 shows a solar burst captured on June 15, 2012 at approximately 20:37:30 UTC. The burst was seen during a thunderstorm that produced numerous lightning strikes which show as the many small spikes. Both of these bursts were verified by other observers on the Radio JOVE mailing list.

June 27, 2012 was a busy day for solar activity. Figure 7.14 shows two bursts, the first at approximately 14:02:30 UTC and the second just after 14:05 UTC. Figure 7.15 shows a closely spaced pair of bursts captured at 14:18 UTC. Figure 7.16 shows a burst captured at 12:38 UTC, just after sunrise. Figure 7.17 shows three bursts beginning

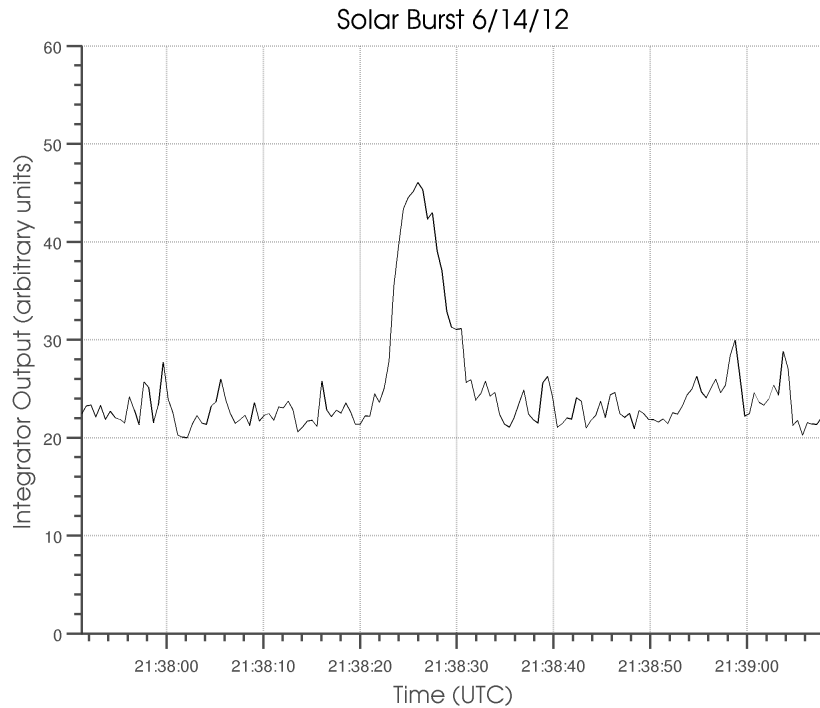


Figure 7.12: Solar burst captured June 14, 2012. It lasts approximately 10 seconds, starting at 21:38:10.

at 19:12:18 UTC and ending at 19:14 UTC. Figure 7.18 shows three bursts beginning at 22:00:30 UTC and ending at approximately 22:01:36 UTC. These bursts were captured during a thunderstorm which produced numerous lightning strikes which caused the many spikes on the plot. All five were confirmed by the Radio JOVE mailing list.

June 28, 2012 was another busy day for solar activity. Figure 7.19 shows a large burst that begins at approximately 02:12 UTC and ends at 02:14 UTC. Figure 7.20 shows multiple very powerful bursts (note the scale on the left) that began at 16:05 UTC and ended at 16:14 UTC. These bursts were associated with an M2 flare from Sunspot 1512, reported by the NASA Solar Dynamics Observatory. Figure 7.21 shows a smaller burst that was captured just as the Sun was beginning to rise on the horizon. Figure 7.22 shows a burst that was associated with a C3 flare that was reported by the NASA Solar Dynamics Observatory at the same time.

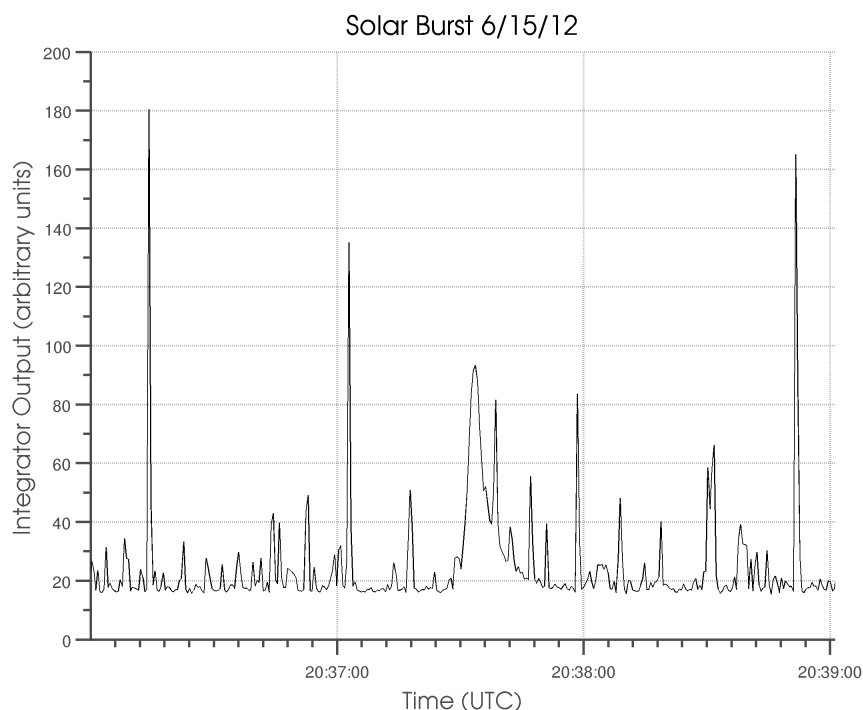


Figure 7.13: Solar burst captured June 15, 2012. This burst was captured while an electrical storm was in the area. The lightning strikes show up as the many small spikes. The solar burst starts at approximately 20:37:30 and lasts until about 20:38:00.

We calibrated the telescope software that used complex data on July 19, 2012. Figure 7.23 was the first solar burst we received after calibration and Figure 7.24 shows a solar burst captured on July 21, 2012.

7.4 Jupiter Bursts

A couple of Jupiter bursts were reported on the Radio JOVE mailing list during the time I was observing with our telescope. Figure 7.25 shows possible S-bursting that we may have captured, although this is unconfirmed. The Radio JOVE list reported an event at this time but no one provided a plot for comparison. Jupiter events are rarely captured during the daytime and all of the events occurred during the day.

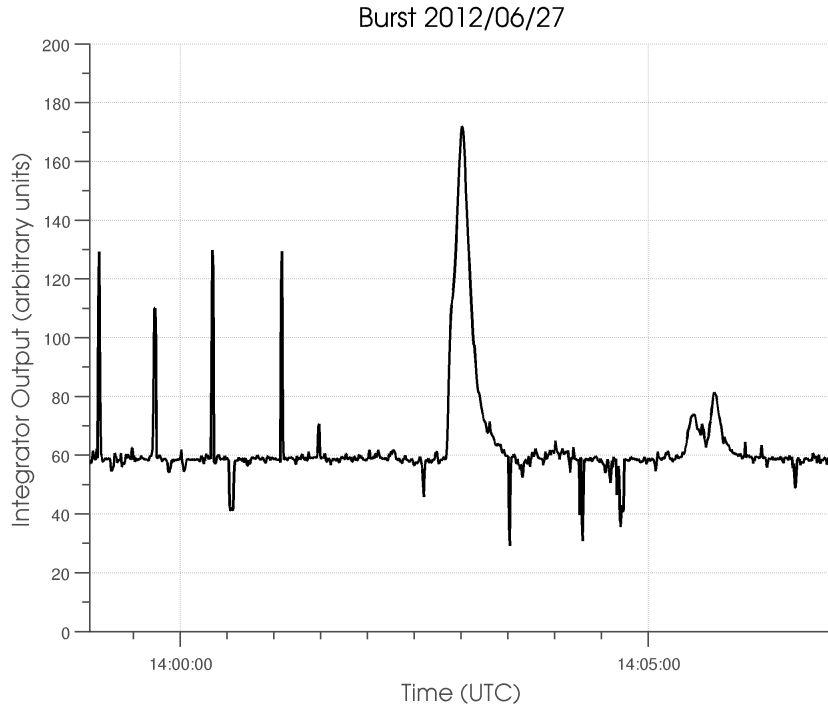


Figure 7.14: Solar bursts captured June 27, 2012. The first burst starts at approximately 14:03 and lasts for about a minute. The second, smaller burst starts just after 14:05 and lasts for about a minute.

In Figure 7.25 the difference in performance between the two channels that I mentioned previously in Section 7.1 is apparent, though the cross-correlation closely follows the northern antenna.

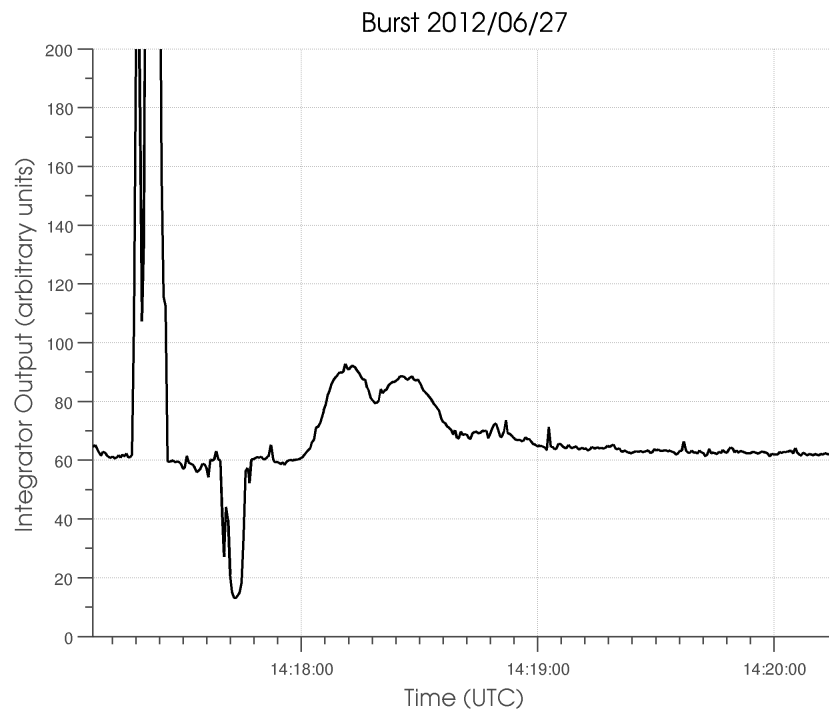


Figure 7.15: Solar burst captured June 27, 2012. This burst starts at about 14:18 and lasts for almost a full minute. The large spike to the left is radio-frequency interference (RFI).

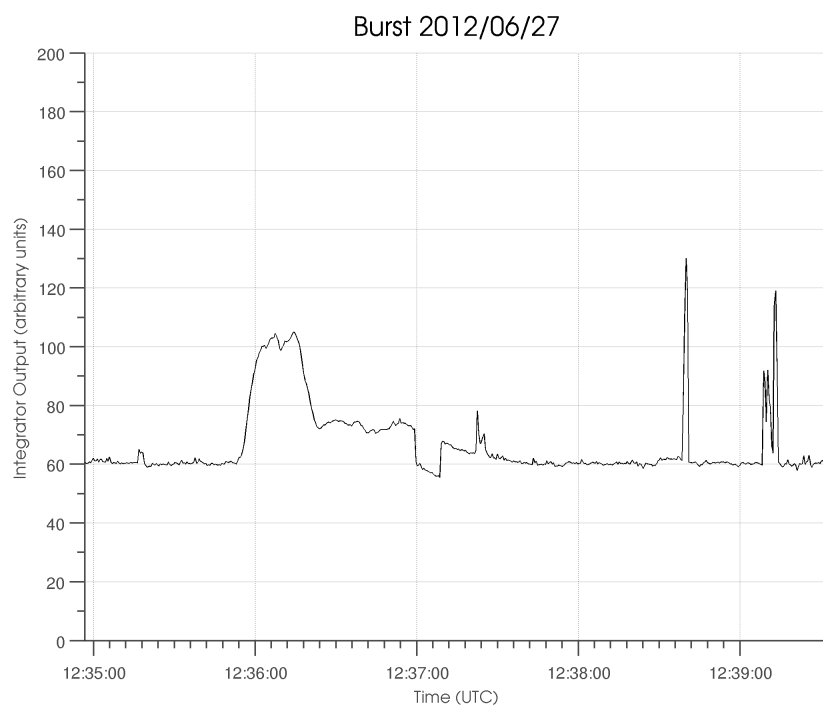


Figure 7.16: Solar burst captured June 27, 2012. The burst starts at 12:36 and lasts for nearly two minutes. We are not sure what caused the abrupt dip in the middle.

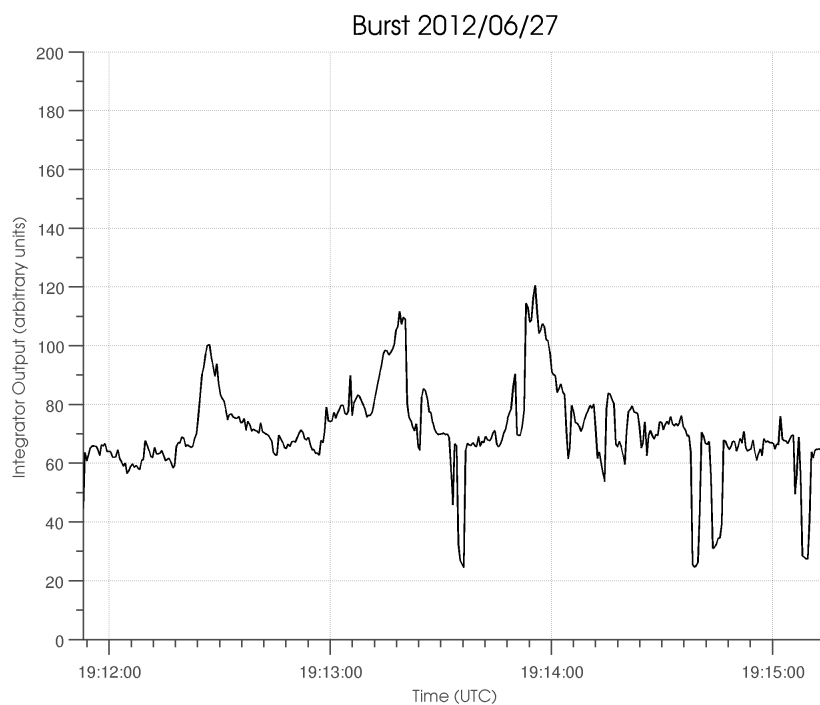


Figure 7.17: Solar bursts captured June 27, 2012. This plot shows three bursts captured over a period of several minutes during a time of high RFI. The first starts at about 19:12:30 and lasts for about 30 seconds. The second starts just after 19:13 and only lasts for 15 seconds. The third burst starts just before 19:14 and lasts for about 15 seconds as well.

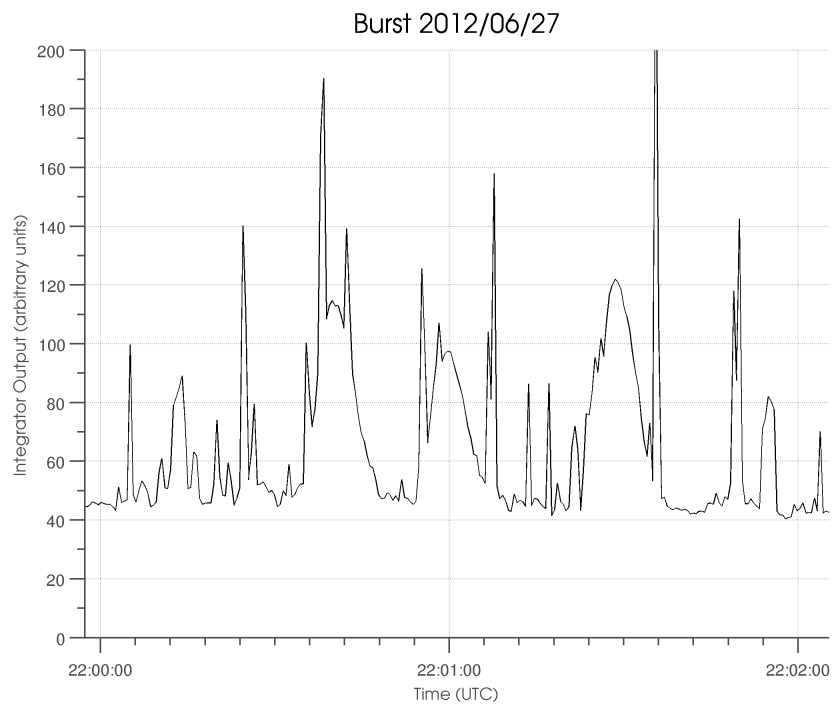


Figure 7.18: Solar bursts captured June 27, 2012. This figure shows three short bursts captured during an electrical storm. The lightning strikes show up as the many small spikes. The first solar burst starts at about 22:00:40 and lasts for about 10 seconds. The second burst starts immediately after and lasts for another 10 seconds. The third burst starts at 22:01:20 and lasts for a final 10 seconds.

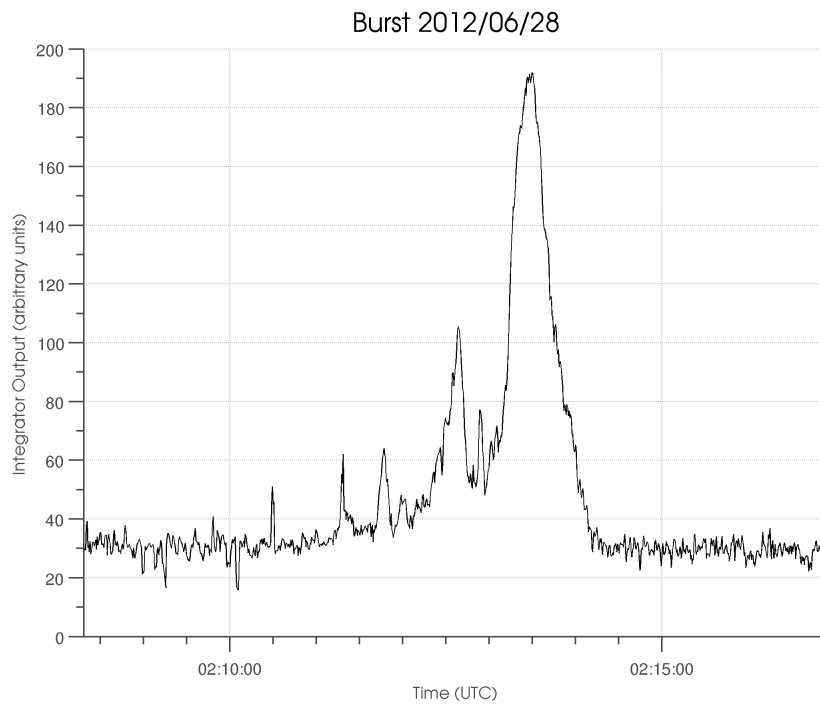


Figure 7.19: Long solar burst captured June 28, 2012. This is a large burst that starts at 02:10 and lasts almost until 02:15. The smaller spikes super-imposed on it are probably RFI.

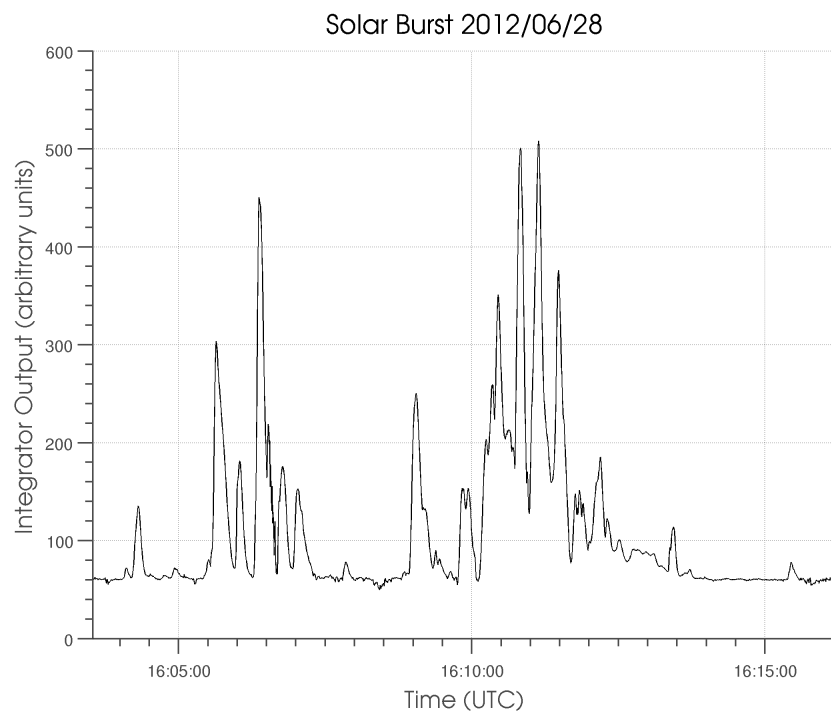


Figure 7.20: Solar bursts captured June 28, 2012, associated with an M2 flare. There are multiple, large bursts (note the scale on the left) that start at 16:05 and continue to 16:15.

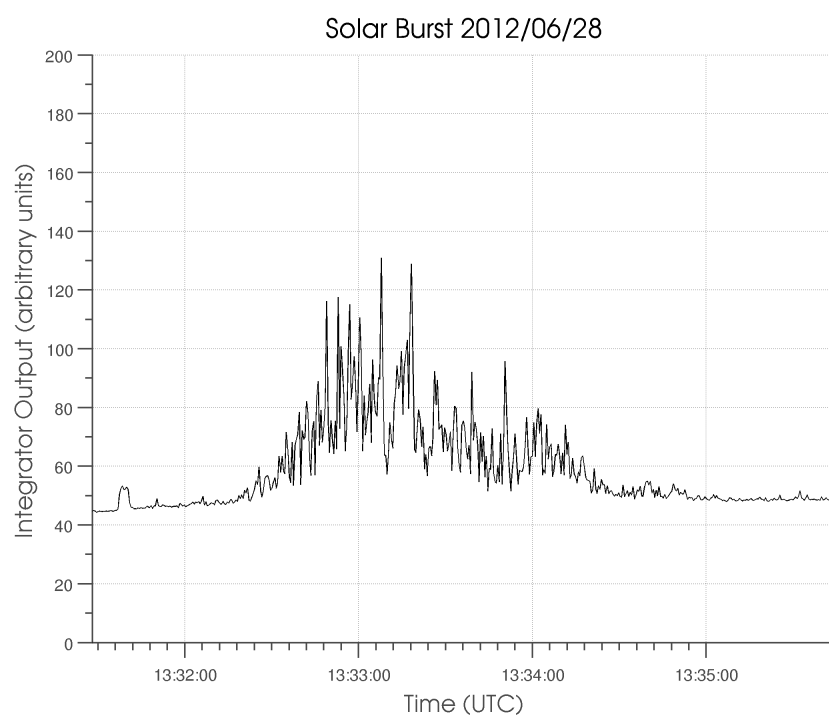


Figure 7.21: Solar burst captured June 28, 2012. This is a strange looking burst that was captured just as the Sun was beginning to rise above the horizon.

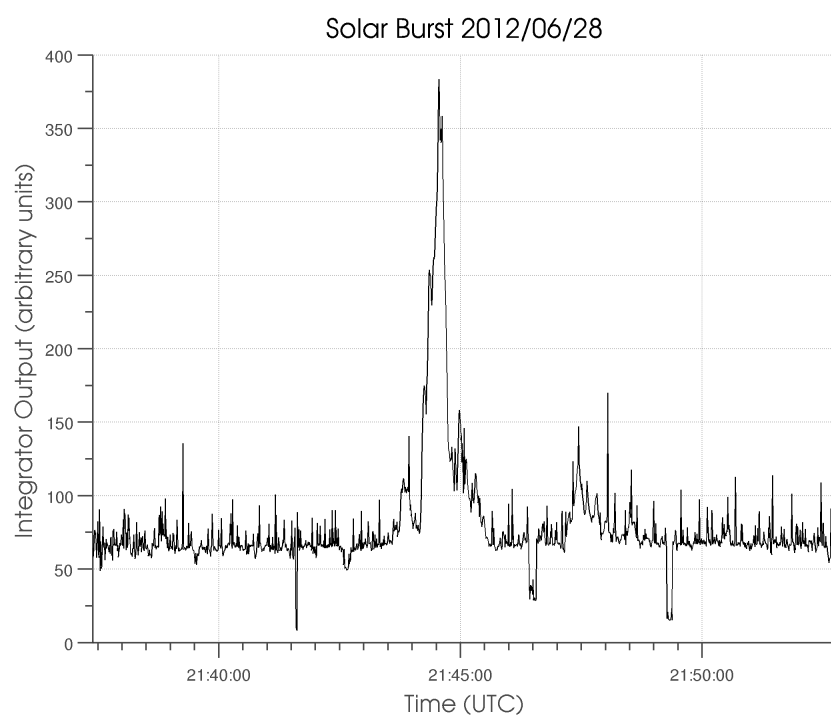


Figure 7.22: Solar burst captured June 28, 2012, starting at about 21:44. This burst is associated with a C3 flare that occurred at the same time.

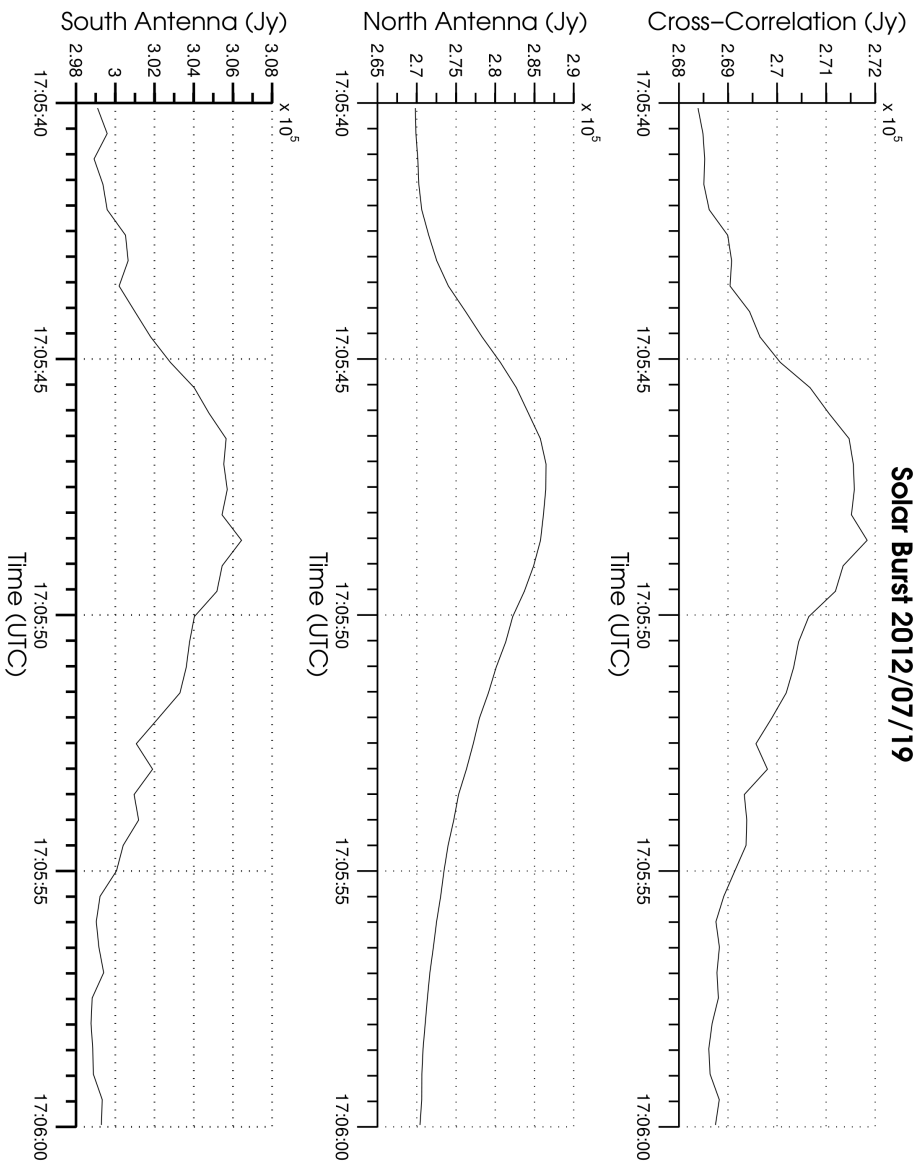


Figure 7.23: Solar burst captured July 19, 2012. It appears that the south antenna picked up some RFI during the burst.

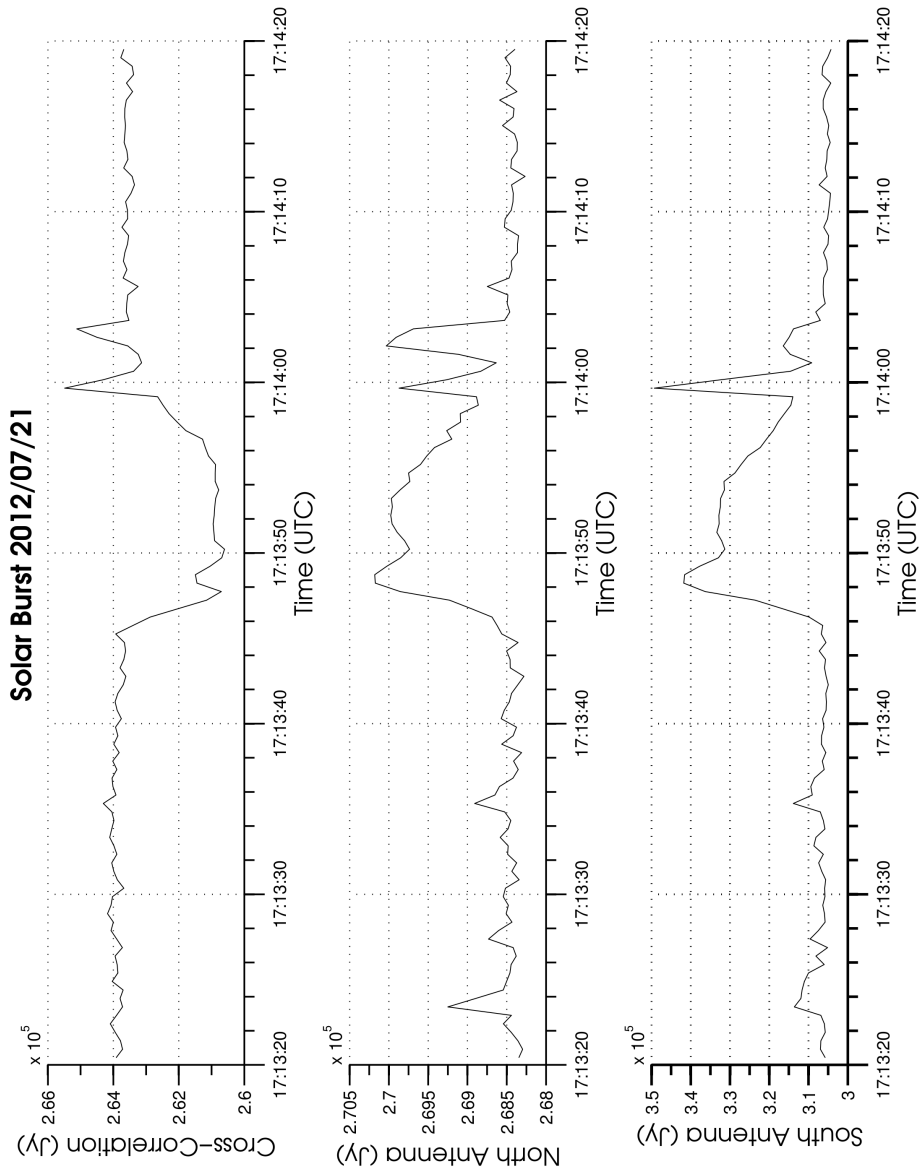


Figure 7.24: Solar burst captured July 21, 2012, starting at 17:13:45. The two spikes near the end are probably RFI. The cross-correlation channel showed a dip instead of a rise, indicating that the Sun was in one of the negative lobes of the interferometer at the time of the burst.

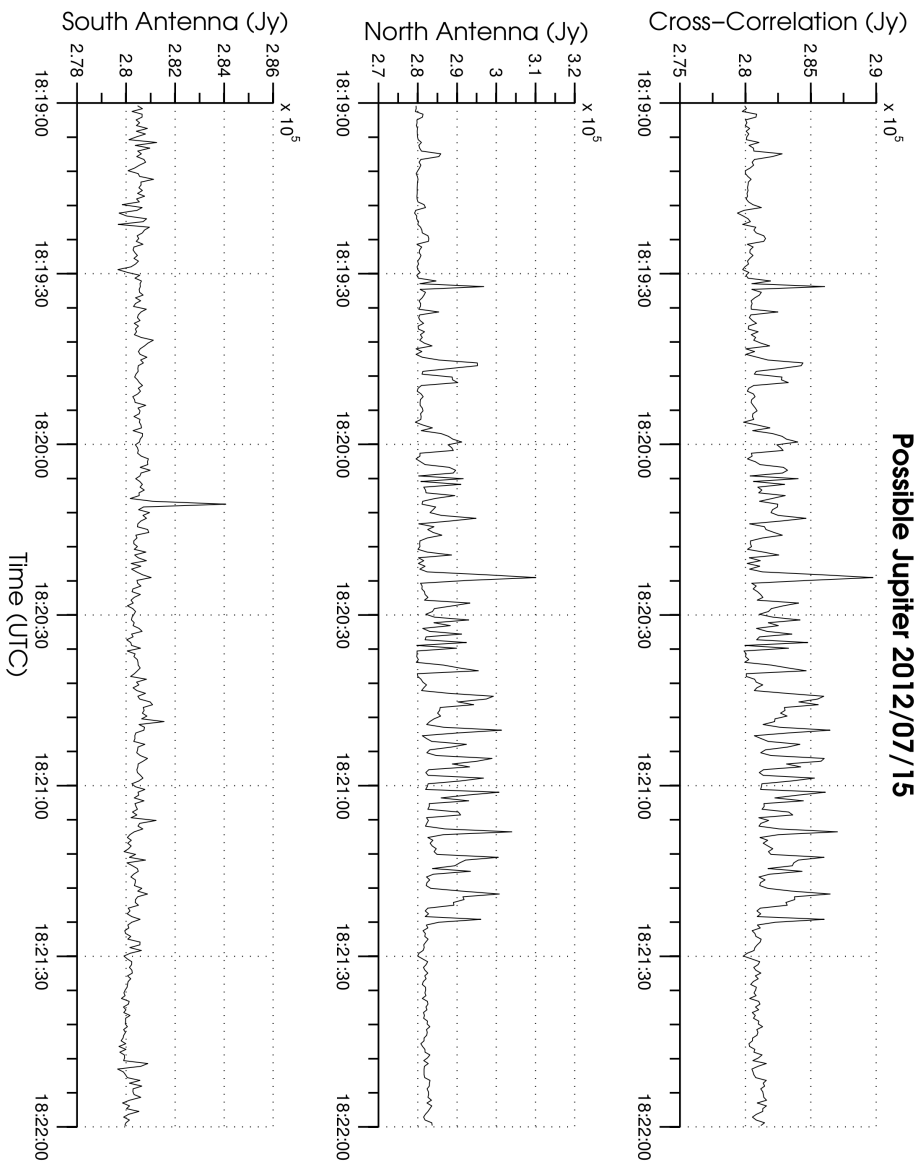


Figure 7.25: Possible Jupiter captured July 15, 2012. The Radio JOVE mailing list reported activity at this time but no plots were provided for comparison.

CHAPTER 8

CONCLUSION

This was a fascinating project and I learned a great deal on RF design and astronomy. There were many times at the end of the project that I reviewed design decisions that I made at the start and would curse myself for failing to do my due diligence. I struggled for a long time to get the telescope to function and was hindered by the poor location and less than ideal antennas. Fortunately towards the end of the project I was allowed to construct a far superior antennas and I really began to get some great results.

One important result of this thesis is that it is possible to do useful radio astronomy in an urban environment. I am hopeful that in the future there will be other experimenters who will be able to make the telescope perform even better.

While we didn't see any emissions from Jupiter I am optimistic that the RF noise will die down when the weather turns cold and we'll be able to see much more than we do now in the summer.

The software receiver works and because the receiver is in software I was able to easily make several upgrades and modifications to correct errors. Had the entire receiver been in hardware making such changes would have been significantly more difficult.

8.1 Future Work

A couple of mistakes that were made should be corrected. First, the calibration function should be switched to use a third-order polynomial. Second, the orientation of the baseline should be investigated. Most interferometers use an east-west baseline but further investigation should be carried out by researching our position on the

Earth and the positions of the sources we wish to receive to determine the optimal baseline orientation.

A recent paper in the journal of Radio Astronomy [15] details a collaboration proposal to use long-wavelength data from the many sites around the world to create a very-long baseline interferometer. Because the samples from the USRP are time-stamped with UTC time our project is ideally positioned to be a founding participant. Indeed this is exactly what my advisor and I had been discussing previously and would make for an excellent project should someone wish to undertake it.

Other avenues for future investigation include implementing a spectrograph, delay tracking, and improving the antenna design.

A spectrograph would allow for easy identification of solar and Jupiter emissions, both of which have a distinct time-frequency characteristic. The initial sampling rate of the USRP is over 100 MSPS which would give the spectrograph a wide bandwidth to monitor. The problem with this is the RF hardware has only a small bandwidth of a few MHz. The band-pass filters would have to be changed to allow for a wider bandwidth for the spectrograph to work with.

Delay tracking could be implemented if we had a longer baseline. I investigated implementing delay tracking for our short baseline but the conclusion I came to was that it wasn't worth the effort, because we would only be able to track with approximately 15° resolution. A longer baseline would improve that significantly.

Improving the antenna would be straight-forward and easy. The design that seems most promising is the Yagi-Uda (see Figure 8.1 and [9] for details). The Yagi-Uda consists of a driven dipole and several director and/or reflector elements, depending on the design. This antenna is much more directive than a simple $\lambda/2$ dipole but is not much more complex or costly. Greater directivity would reduce the amount of Earth-based interference that we currently receive.

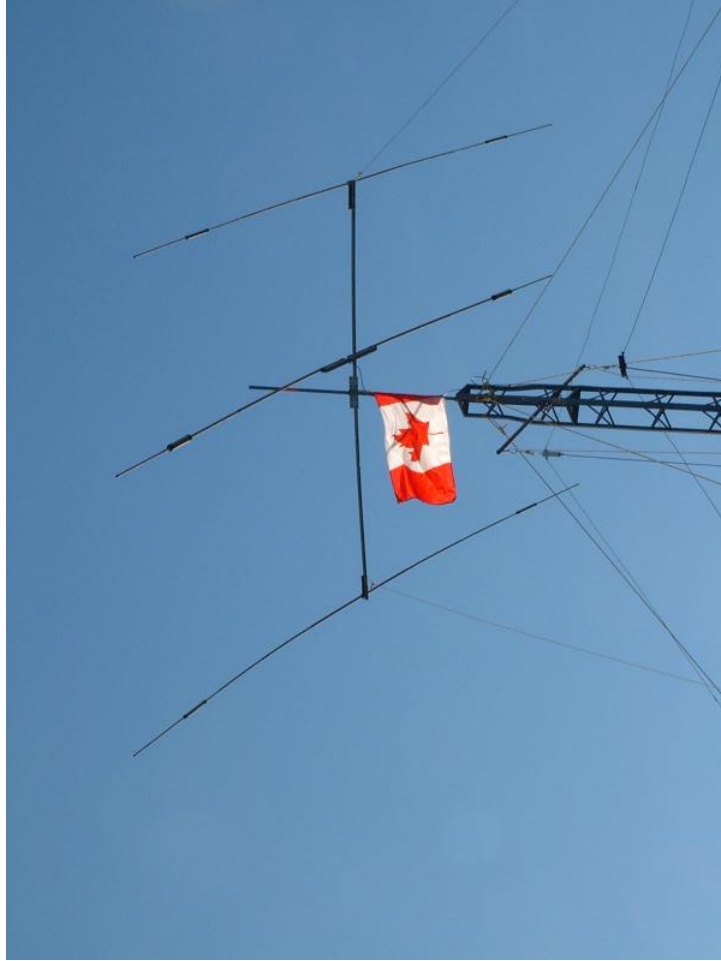


Figure 8.1: A Yagi-Uda antenna photo, published on Wikipedia. This antenna design is an ideal candidate for an improvement over the current $\lambda/2$ dipole.

I truly hope that this thesis, software, designs, and the data we capture is useful to others. By open-sourcing the software and the hardware our vision is that others will be able to freely use my work and improve upon it for future users. Questions, comments, and criticism is always welcome at mike@dietfig.org, though I must warn you I am still blundering through this fascinating area!

REFERENCES CITED

- [1] David Brodrick, Tim Kennedy, Steven Tingay, and Daron Brooke. 20-mhz interferometer, October 2002. URL <http://www.atnf.csiro.au/news/newsletter/oct02/simple.htm>.
- [2] Texas Instruments. *ADS62P44 Datasheet*, 2009.
- [3] Ettus Research. *USRP N200/N210 Networked Series*.
- [4] A. Richard Thompson, James M. Moran, and George W. Swenson Jr. *Interferometry and Synthesis in Radio Astronomy*. Wiley-Interscience, second edition, 2001.
- [5] John D. Kraus. *Radio Astronomy*. Cygnus-Quasar Books, second edition, 1986.
- [6] Constantine A. Balanis. *Antenna Theory*. Wiley, 2005.
- [7] J. P. Wild. The radio emission of the sun. *Radio Astronomy Today*, 1963.
- [8] E. K. Bigg. Influence of the satellite io on jupiter’s decametric radiation. *Nature*, 1964.
- [9] R. Dean Straw, editor. *The ARRL Antenna Book*. The ARRL, Inc., 2003-2005.
- [10] S.W. Ellingson, J.H. Simonetti, C.D. Patterson, V. Venugopal, S. Cutchins, and D.W. Taylor. Annual progress report on nsf award no. ast-0504677: Ati: Searching for low-frequency radio transients. 2006.
- [11] Mini-Circuits. *RVA-33+ Datasheet*.
- [12] Pasternack. *RG-58C/U Datasheet*.
- [13] Ron Block. Lightning protection for the amateur radio station. *QST*, 2002.
- [14] David Pozar. *Microwave and RF Design of Wireless Systems*. Wiley, 2001.
- [15] Ray Fobes, Neal Vinson, and Jim Campbell. Long wavelength astronomy - a collaboration proposal for the radio astronomy community. *Radio Astronomy*, May 2012.

APPENDIX A - LICENSES

A.1 Hardware License

All hardware is Copyright ©2011, 2012 Mike Roddewig. All rights reserved.

All hardware designs and files are licensed under the TAPR Open Hardware License v1.0, a copy of which is located at <http://www.tapr.org/OHL>.

A.2 Software License

FPGA software is based on software written by Ettus Research, LLC Copyright ©2011, 2012. Tektronix library is Copyright ©2006 Steve D. Sharples <<http://optics.eee.nottingham.ac.uk/vxi11/>>.

All remaining software is Copyright ©2011, 2012 Mike Roddewig. All rights reserved.

The telescope software is free software: you can redistribute it and/or modify it under the terms of the GNU General Public License v3 as published by the Free Software Foundation.

The telescope software is distributed in the hope that it will be useful, but WITHOUT ANY WARRANTY; without even the implied warranty of MERCHANTABILITY or FITNESS FOR A PARTICULAR PURPOSE. See the GNU General Public License for more details.

You should have received a copy of the GNU General Public License along with this program. If not, see <<http://www.gnu.org/licenses/>>.

APPENDIX B - SCHEMATICS

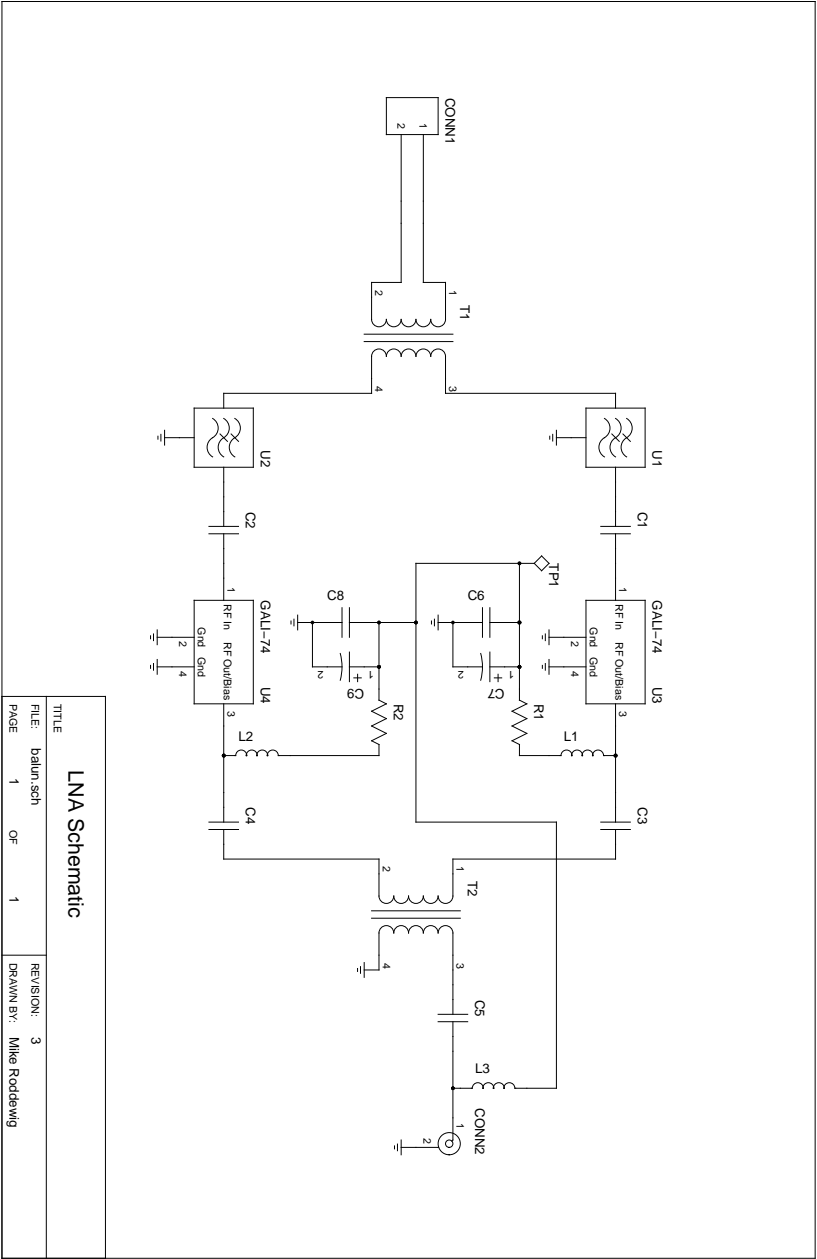


Figure B.1: LNA Schematic

Table B.1: LNA Bill of Materials

Reference Designator	Type	Value	Manufacturer	Part Number
C1, C2, C3, C4, C5	Capacitor	1 μ F	Murata	GRM188R60J105KA01D
C7, C9	Capacitor	10 μ F	Kemet	T491A106M020AT
C6, C8	Capacitor	0.1 μ F	Murata	GRM31C5C1E104JA01L
R1, R2	Resistor	78.7 Ω	Vishay Dale	CRCW201078R7FKEF
U1, U2	Lowpass Filter		Mini-Circuits	SCLF-44+
U3, U4	Amplifier		Mini-Circuits	GALI-74+
L1, L2, L3	RF Choke	1.3 μ H	Coilcraft	4310LC
T1	RF Transformer		Coilcraft	WB13-1TL
T2	RF Transformer		Coilcraft	WBC2-1TLB
CONN1	Binding Posts		Pomona Electronics	4243-0
CONN2	SMA Connector		Amphenol	132134

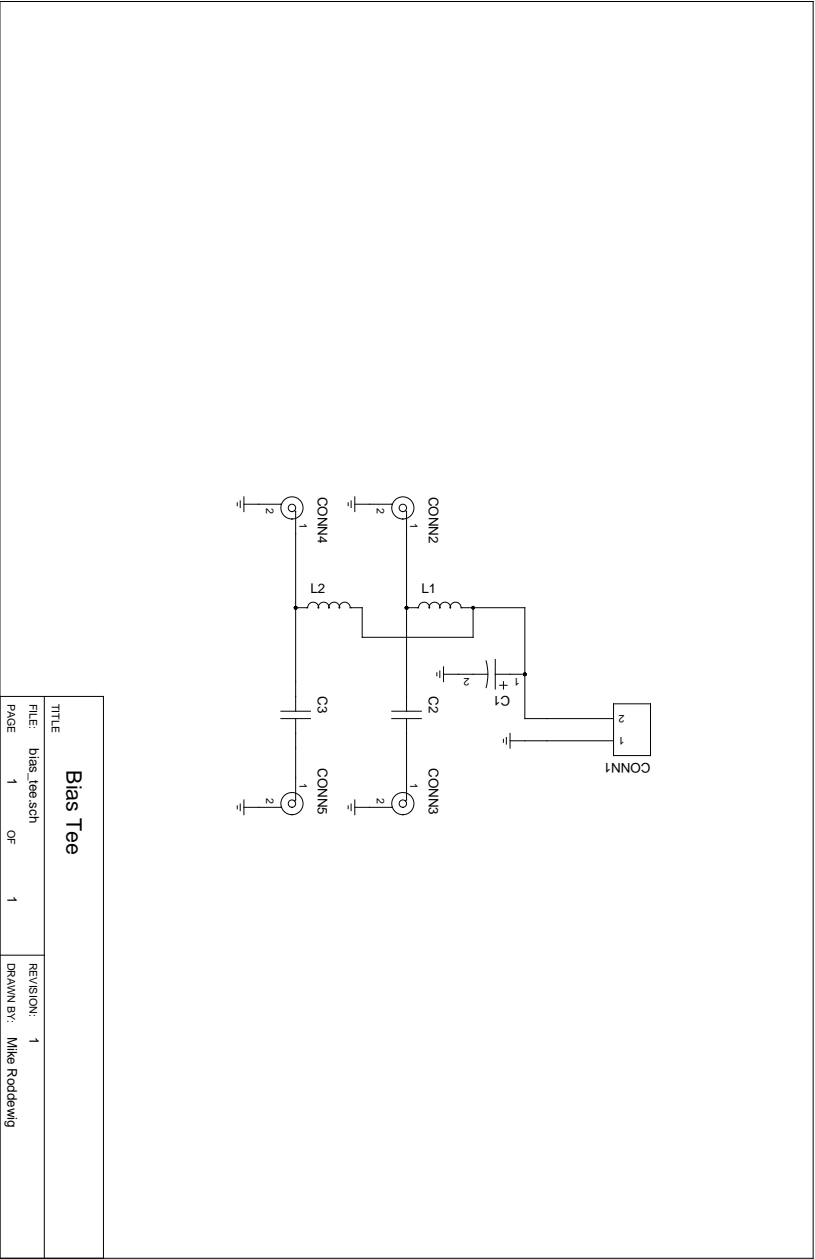


Figure B.2: Bias Tee Schematic

Table B.2: Bias Tee Bill of Materials

Reference Designator	Type	Value	Manufacturer	Part Number
C1	Capacitor	10 μ F	Kemet	T491A106M020AT
C2, C3, C4, C5	Capacitor	1 μ F	Murata	GRM188R60J105KA01D
L1, L2	RF Choke	1.3 μ H	Coilcraft	4310LC
CONN1	Terminal Block		TE Connectivity	282836-2
CONN2, CONN3, CONN4, CONN5	SMA Connector		Amphenol	132134

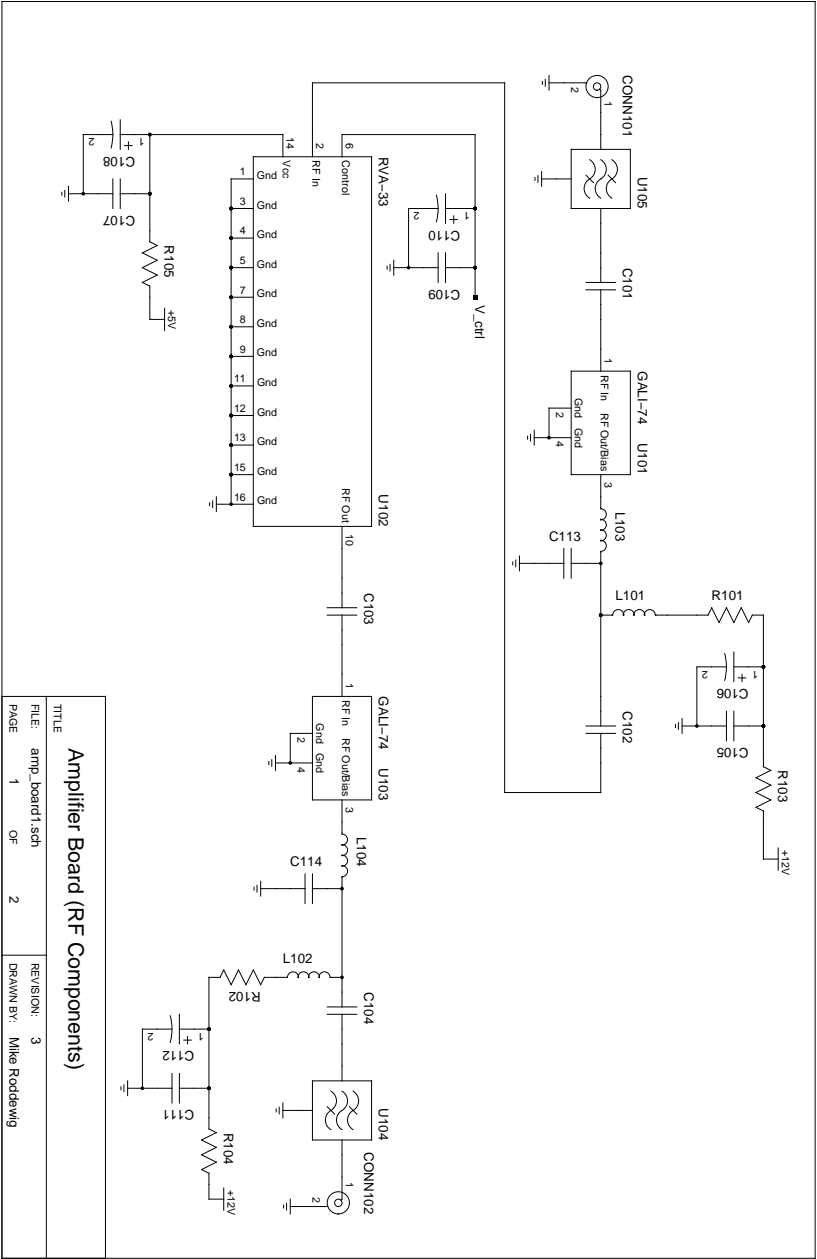


Figure B.3: Amp Board Schematic (RF Components)

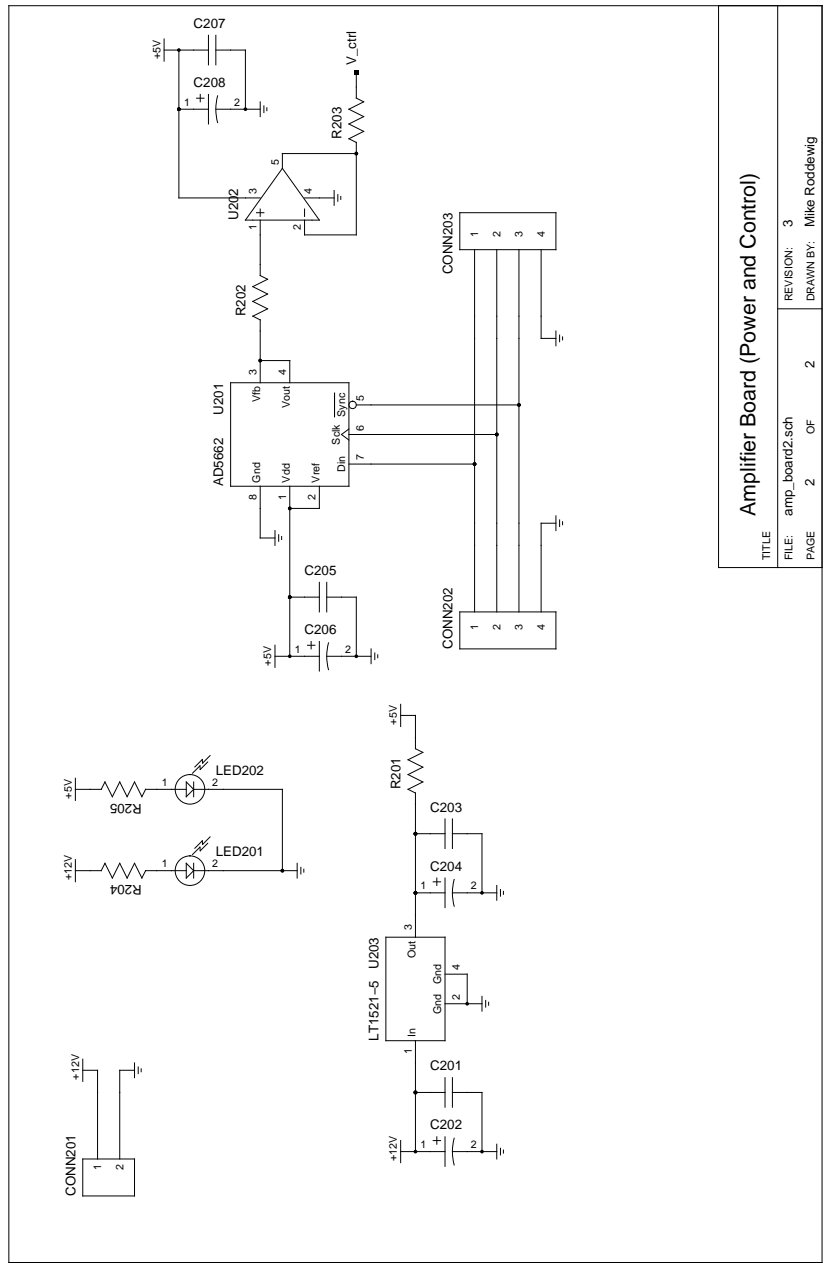


Figure B.4: Amp Board Schematic (Power and Control Components)

Table B.3: Amplifier Board Bill of Materials

Reference Designator	Type	Value	Manufacturer	Part Number
C106, C112, C202	Capacitor	10 μ F	AVX	TCJA106M016R0200
C108, C110, C204, C206, C208	Capacitor	10 μ F	AVX	TCJA106M006R0300
C101, C102, C103, C104	Capacitor	1 μ F	Murata	GRM188R60J105KA01D
C105, C111, C201	Capacitor	0.1 μ F	TDK	C1608X7R1C104K
C107, C109, C203, C205, C207	Capacitor	0.1 μ F	Johanson Dielectrics	6R3X14W104MV4T
C113, C114	Capacitor	110 pF	Murata	GRM1555C1H111JA01D
L101, L102	RF Choke	1.3 μ H	Coilcraft	4310LC
L103, L104	Inductor	0.27 μ H	TDK	MLG1005SR27J
R101, R102	Resistor	90.9 Ω	Panasonic	ERJ-12SF90R9U
R103, R104, R105, R201, R202, R203	Resistor	0 Ω	Stackpole	RMCF0603ZT0R00
R204	Resistor	390 Ω	Panasonic	ERJ-14YJ391U
R205	Resistor	120 Ω	Panasonic	ERJ-8GEYJ121V
LED201, LED202	LED		Lumex Opto	SSL-LXR1612GD
CONN101, CONN102	SMA Connector		Amphenol	132134
CONN201	Terminal Block		TE Connectivity	282836-2
CONN202, CONN203	Standard Male Header			
U101, U103	Amplifier		Mini-Circuits	GALI-74+
U102	Variable Attenuator		Mini-Circuits	RVA-33+
U104, U105	Bandpass Filter		Mini-Circuits	SXBP-20R5+
U201	DAC		Analog Devices	AD5662BRJZ-2REEL7
U202	Op-Amp		Analog Devices	AD8391ARTZ-REEL7
U203	Linear Regulator		Linear Technology	LT1521IST-5#PBF

APPENDIX C - BOARD DRAWINGS

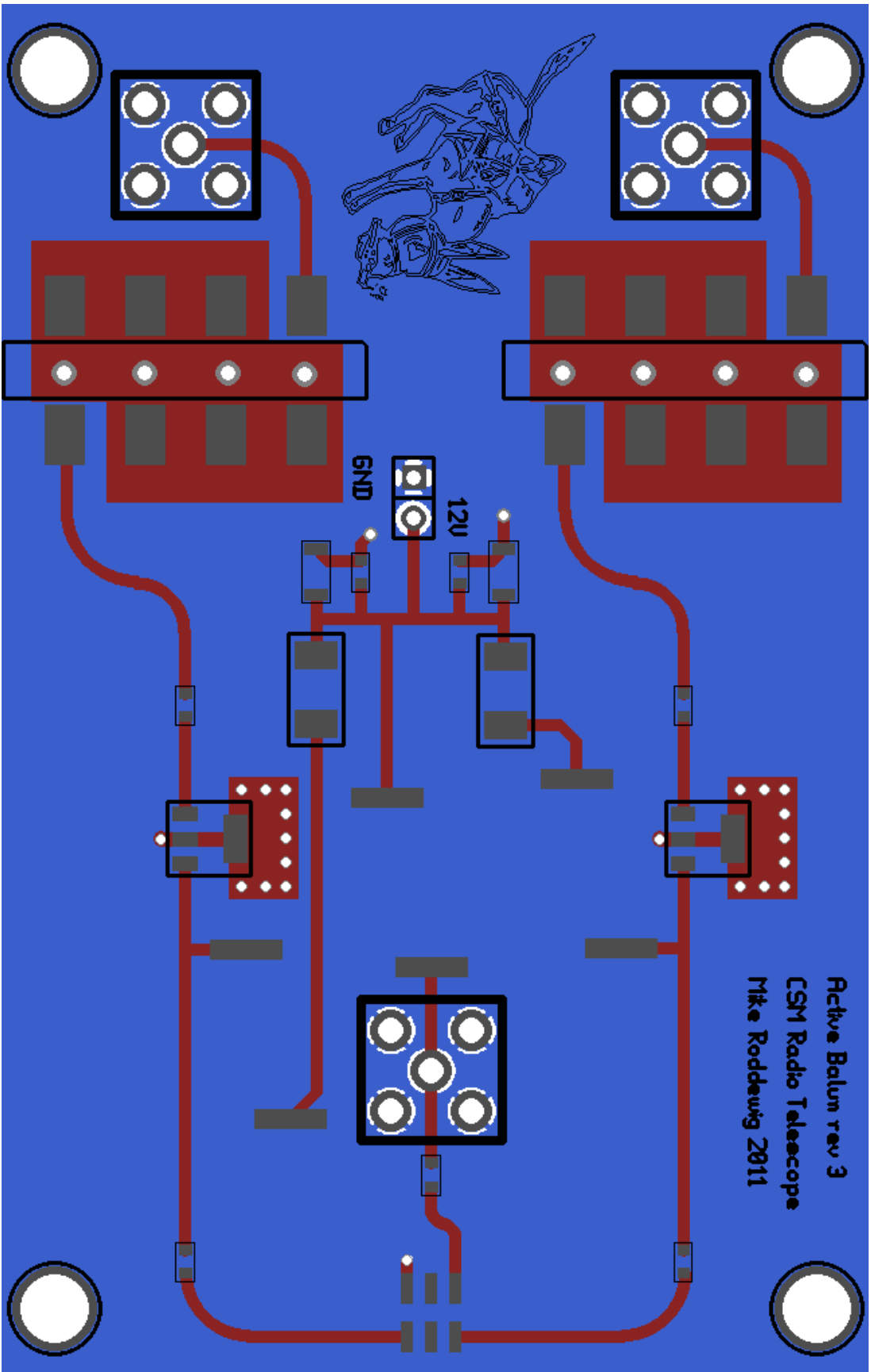


Figure C.1: LNA Board Drawing

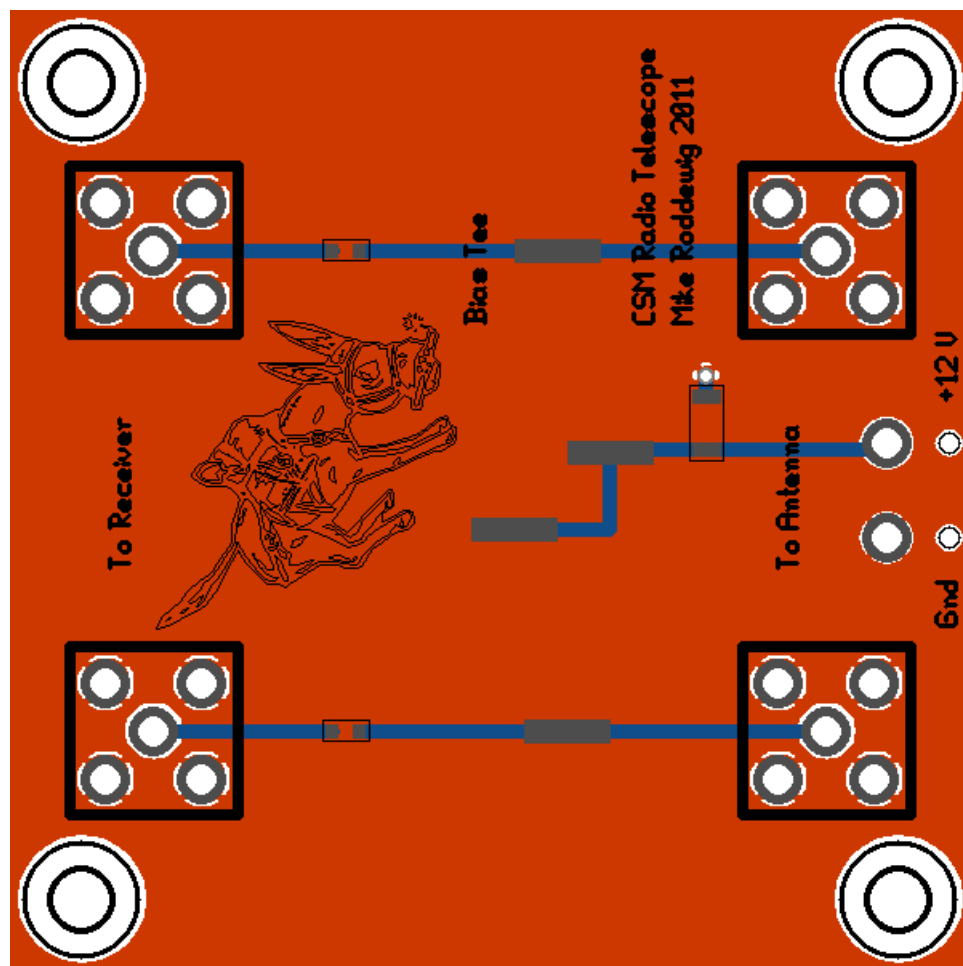


Figure C.2: Bias Tee Board Drawing

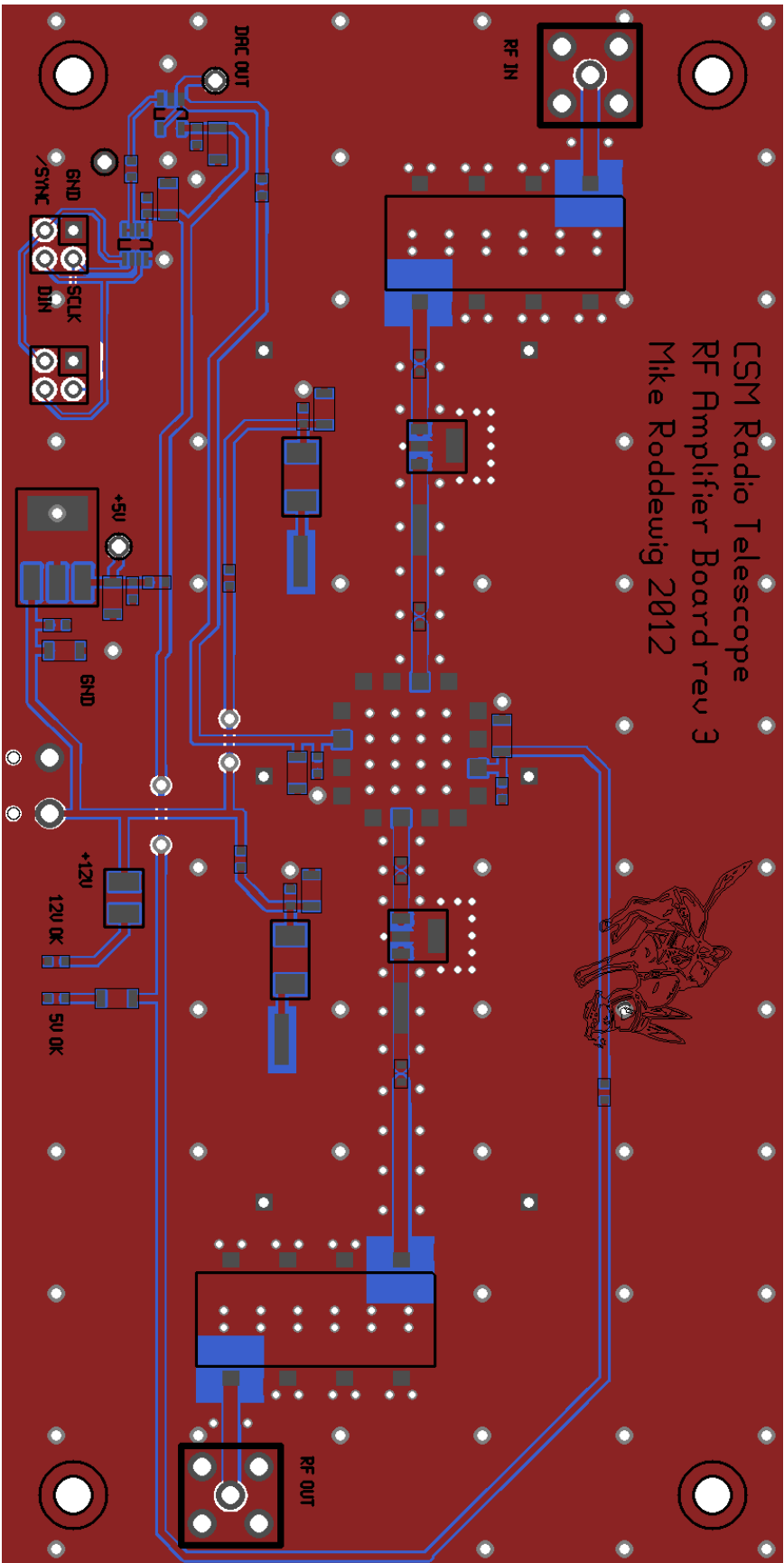


Figure C.3: Amp Board Drawing